Korean J. Chem. Eng., **28**(4), 987-1008 (2011)
DOI: 10.1007/s11814-011-0051-3

INVITED REVIEW PAPER

The principles and applications of nano-diagnosis system for a nano-biosensor

Jong Min Kim*, Sang-Mok Chang*, Hiroshi Muramatsu, and Karube Isao**,†**

*Department of Chemical Engineering, Dong-A University, 840 hadan-dong, Saha-gu, Busan 604-714, Korea
**Department of Bioscience and Biotechnology Tokyo University of Technology,
1404-1, Katakura, Hachioji, Tokyo 192-0982, Japan
(*Received 13 January 2011 • accepted 2 March 2011*)

Abstract−In this review, the basic principles and research trends of biosensors are briefly described and a nano-sensing system applying QCM (quartz crystal micro-balance), nano-diagnosis methods by AFM (atomic force microscopy) and SNOAM (scanning near-field/atomic force microscopy) is discussed intensively. The principle, construction, and applications of piezoelectric crystal sensors as a universal sensor are reviewed. This review is focused mainly on liquid phase applications, such as immune-sensors, gelation detecting sensors, and cultured cell monitoring sensors. The principle of nano-diagnosis based on the AFM or SNOAM techniques is described in detail. Finally, the binding affinity of peptide probes to proteins using AFM and the visualizing of a hybridized PNA probe on a DNA molecule using SNOAM are evaluated and discussed.

Key words: Biosensors, Nano-sensor, Quartz Crystal Microbalance, Nano-diagnosis, Scanning Probe Microscopy

INTRODUCTION

As the quality of life has improved, simple measuring instruments that can easily measure various chemicals are needed in health management, environmental conservation, agriculture, and the chemical industry in accordance with the required demands. For safety and quality management in the industrial fields, the demand for quickly and accurately measuring various chemicals via an on-line method has been increasing. As well, the desire for self-diagnosis of one's own health and self-examining the safety of environment has been gradually increasing. And with an increasingly aging society, the remote diagnostics of the elderly are also needed. Furthermore, the desire for self-assessing the safety and quality of the foods has been gradually increasing. Various kinds of chemicals coexist in the areas of health care, environmental protection, agriculture, and chemical industry, and many physico-chemical devices are used to measure these chemicals. In general, complex operations and long operational time are required to monitor various harmful chemicals. Therefore, a direct, quick and simple device to monitor these chemicals is intensively needed.

Sensors measure certain physical or chemical quantities from the external environment, converting them into electrical signals. A sensor that measures physical quantities such as light, temperature, and pressure, converting them into electrical signals is called a physical sensor, and a sensor that measures the species and concentration of specific chemicals, converting them into electrical signals is called a chemical sensor. Unlike physical sensors measuring one physical parameter at a limited time, chemical sensors that selectively measure a certain target chemical in the mixture of several compounds have to be improved in the respect of both the selectivity and the sensitivity.

†To whom correspondence should be addressed.
E-mail: karube@bs.teu.ac.jp

Mankind has been able to have powerful tools of measuring systems due to the development of science and technology. Living organisms have become one of models in new studies for the development of science and technology. Living organisms, including human beings, basically receive information from the surrounding environment via the five sense organs and immune reaction, and respond to the environment. The sensor system mimicking living organisms has been considerably studied, but has not yet been developed to a satisfactory level. This is attributed to the fact that the information detected by the living organisms is a mixture of physical and chemical parameters of various compounds, which cannot be easily measured and analyzed. To measure selectively a specific chemical from the mixture of several kinds of chemicals, a sensor should specifically respond to the chemical of interest. Some chemical sensors are already practically used, but their function for molecular recognition is not yet sufficient. To manufacture chemical sensors with the function of accurate identification of chemicals, the biological system should be considerably mimicked. Biological systems ranging from unicellular organisms to multi-cellular organisms have sensory organs responding to various stimuli. Thanks to this, living organisms can maintain their body, and measure the environmental hazards, or protect the body from the enemy.

Biosensors, which use biological principles to identify chemicals based on the modeling of these sensory organs, are one of the achievements of biotechnology and draw attention as a simple alternative to the conventional complex analytical instruments in various fields. Biosensors use biochemical materials as selective receptors or detect biochemical materials.

The basic researches on biosensors have focused on the development of new receptor materials and detection methods, whereas the practical researches have mainly focused on performance improvements such as high sensitivity, safety, reliability, and reproducibility. Sufficient reviews of biosensors have already introduced and many good books already published. Therefore, in this review,

we will briefly summarize the basic principles and research trend of biosensors, and introduce the measuring principles and applications of the biosensors using quartz crystal, AFM and SNOAM.

BASIC PRINCIPLES AND RESEARCH TREND OF BIOSENSORS

Biosensors are devices that detect and quantify target material by combining the physicochemical instruments and biological selective materials such as enzyme, antibody, cell, or various tissues. The physicochemical instruments are called transducers, and biological selective materials are called receptors. The specific selectivity of the chemical sensors depends on the selective materials synthesized for specific binding. On the other hand, that of the biosensors depends on the selectivity of the materials derived from the biological organisms. Biosensors respond selectively to the target materials via a receptor and convert biological signals generated by the resultant biochemical reaction into electrical signals using a transducer. In a broad concept, biosensors include sensors that mimic biological systems even without the use of biological materials, such as the smell sensor that mimics the olfactory organ and the taste sensor that mimics the taste organ. Among biological materials, enzymes have extremely good properties so that they selectively distinguish and react with specific materials called substrates to play a role as an *in vivo* catalyst. Some methods that measure a specific chemical using an enzyme have been used in analytic chemistry. Thanks to the recent development of biotechnological industries, various enzymes have been produced and are commercially available. The enzymes have been widely used as a reagent in the fields of medical and food analysis and many improvements including that of complex manipulation have been made. As most enzymes are water-soluble, careful enzyme immobilization is required for stability in a repeated use. Since the late 1960s, studies on enzyme immobilization techniques have been vigorously conducted. Clark first proposed the principle of the enzyme sensor that combines an enzyme and an electrochemical device [1]. Then, in 1966, Updike and Hicks manufactured the first glucose sensor using an immobilized enzyme [2]. This sensor had the oxygen electrode with an oxygen-permeable membrane coated with the enzyme membrane wherein glucose oxidase was immobilized onto polyacrylamide gel.

Various physico-chemical devices have been used as a transducer, among which the electrochemical electrode has been used predominantly. The electrode is used to analyze the electrical signals generated by an enzyme reaction [3,4]. Chemicals that are produced or consumed in an enzyme reaction can be also measured by semiconductor technology. For example, hydrogen ion or hydroxyl ion generated in an enzyme reaction can be measured with ion selective field effect transistor (ISFET) [5]. As a temperature change is normally accompanied with biochemical reactions, a sensor that measures temperature change with a thermistor was also developed [6]. In addition, in the case wherein an enzymatic reaction is associated with the reactions of biochemical luminescence, the degree of the light-emitting can be measured by using a photon counter or a photodiode [7]. When an enzymatic reaction is accompanied with changes in the mass due to the specific binding such as antigen-antibody reactions, the mass change can be analyzed by quartz crystal micro-balance (QCM) [8], surface plasma resonance (SPR) [9], and cantilever based sensors [10,11]. In addition, enzyme reactions can be measured by using sound waves, microwaves, and laser beams. Furthermore, like the chemical receptors of human beings, it is possible to develop an artificial membrane wherein membrane potentials can be directly changed by chemical stimulants. As mentioned above, biosensors with a wide variety of principles can be produced using specific transducers [12-14].

Various kinds of biosensors can be also produced based on the type of biological materials. In addition to enzymes, many substances that can distinguish chemicals exist in living organisms. Antibodies, antigens, or receptors have the ability to recognize specific chemicals. All of them could be composed as sensors by combining various electrodes and transducers that were already described in above. Various sensors, such as receptor sensors using receptors [15], immune sensors using antigen/antibody reactions [16-18], cell sensors using animal and plant cells [19-21] and tissue sensors using animal and plant tissues [22], have been already developed based on these principles. Since SELEX (systemic evolution of ligands by exponential enrichment), a technology for identifying aptamers, was first introduced by Larry Gold's team in 1990, aptamer-based biosensors have been actively conducted [23,24]. An aptamer consists of single nucleotide sequence DNA or RNA and responds to a biological material selectively. Most biological materials are water soluble. Thus, the immobilization of aptamers is needed to use them as a component of sensors in the same manner as enzymes. As many good books on the immobilization methods have been published, refer to them for detailed information.

Interdisciplinary researches, including life sciences, chemistry, physics, electrical engineering, mechanical engineering and semiconductor engineering, have been actively conducted in the recent biosensor researches. Bio-diagnostic techniques, such as a biochip and a lab-on-a-chip, are the most developed and applied fields among the interdisciplinary researches. Conventional biosensors conduct quantitative and qualitative analyses for one chemical at a time, whereas biochip is a sensor system expanded with the concept of a chip, wherein tens of thousands DNAs or proteins are arrayed and attached on a plate at regular intervals using a semiconductor fabrication technique, and target materials are processed to analyze the binding patterns [25-27]. A lab-on-a-chip is a sensor system wherein the process, collection and analysis of samples are integrated and conducted on a single chip to diagnose diseases. As lab-on-a-chip became smaller and lighter, a small amount of samples could be processed and removed quickly and easily, and it became also portable [28,29]. Biochips are classified into DNA chips [25-27], protein chips [30-34], cell chips [35,36], and neuron chips depending on the use of biological materials and systemization level. A biochip is a biological micro-chip that can analyze gene function, disease-related gene, gene expression, protein distribution and response patterns.

A nano-biosensor or a nano-biochip is a sensor that has been improved to perform functions that were not possible with the conventional biosensors and biochips by fusing nanotechnology and the existing biosensors or biochips. Nano-materials that are applied to the sensors include a variety of materials such as nanowire [37-40], carbon nanotube [41-44], nano fiber [45-49], nano particles [50-54], metal nano-pattern and ion-channel material [41,55,56]. As many good reports on this study have been published, please refer to them for more information.

NANO-SENSING SYSTEM USING QUARTZ CRYSTAL MICRO-BALANCE

Quartz crystal has been widely applied to electronic devices as a source of precise reference signal using the piezoelectric effect of the crystal. Quartz crystals are typically divided into AT-cut, GT-cut, and CT-cut, and they are diversely used depending on specific application fields. In general, AT-cut quartz crystal is used as a sensor transducer. The temperature dependence on the resonant frequency of quartz crystal is important in the application of chemical sensors, and the sensitive temperature characteristic appears depending on the cutting angle to the axis. For the AT-cut crystal, the characteristic of the resonant frequency is stable in the temperature range from 0 ºC to 40 ºC, which is important for various chemical sensors or gas sensors applied at room temperature. Quartz crystal sensors are used as a highly sensitive mass sensing device using the correlation of the resonant frequency characteristics with the mass absorbed on the substrate plate. The high stability of the resonant frequency is possible because the Q value (the ratio of the wavelength to the wave height) of the quartz crystal is high [57]. Quartz crystal microbalance (QCM) is an analytic device that can detect the mass change of approximately 1 ng by measuring the resonant frequency of the quartz crystal. Since the quartz crystal was theoretically proven by Sauerbrey for its application as an analytical device, it has been mainly used for gas analysis [58-60]. After Kanazawa et al. experimentally proved that the oscillation of quartz crystal is possible in a liquid phase, the application of the quartz crystal as an analytical device has been extensively researched [61]. In particular, we presented the concept of the resonant resistance that can analyze the dynamic behavior of coated thin films on the surface of the quartz crystal. Thus, the quartz crystal microbalance was further developed as quartz crystal analyzer (QCA). Currently, it known as a measuring device for fine mass and the viscoelastic change, and various applications using its properties have been reported in the areas of immune assay, the observation of gelation reactions, electrochemical experiments, the observation of the changes in the rheological properties of organic thin films, and viscoelastic measurements in the nano-meter area [8,62-73].

To improve the recognition function and analyzing reliability of the quartz crystal, researches obtaining various kinds of information simultaneously by combining several instruments have been recently vigorously conducted. To analyze viscoelasticity of polymer films, the quartz crystal resonator (QCR) and differential scanning calorimetry (DSC) were simultaneously used by the authors' group [69,70]. In addition, morphological changes were also observed using AFM [71-74]. Studies on the change in viscoelastic properties in the mirco-area by integrating QCR and atomic force microscopy, on the change in the permeability of the PPy films based on oxidation-reduction reactions by integrating QCR and UV-visible spectroscopy, and on the analysis of the morphological structure of thin films based on the viscoelastic change using QCR and AFM were reported. A system simultaneously analyzing QCR and surface plasmon resonance (SPR) responses is actively being researched to improve the reliability and sensitivity of the sensor system [73]. In the current review, the principles of the measurement, the concrete examples of nano-sensing using the quartz crystal and the possible applications in biological science will be briefly described.

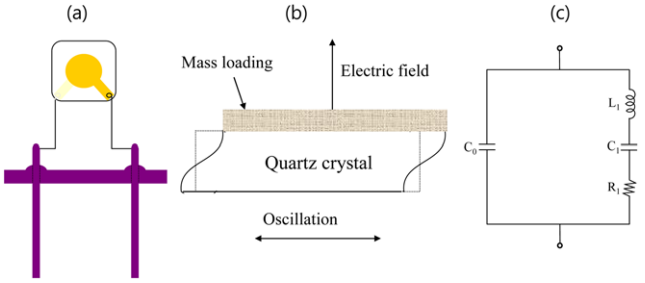

Fig. 1. A schematic diagram of AT-cut quartz crystal (a). The oscillation model of the piezoelectric quartz crystal in the shear vibration (b). An electrical equivalent circuit of the quartz crystal (c).

1. Principle of Nano-sensing Based on the Quartz Crystal

A typical schematic diagram of an AT-cut quartz crystal (a), its oscillation model (b), and an electrical equivalent circuit (c) are shown in Fig. 1.

The relationship between a resonant frequency change and a change in the elastic film mass on the quartz crystal has been derived by Sauerbrey based on an idealized physical mode [58]:

$$\Delta F = -\Delta m F^2/(\mu\rho_Q)^{1/2} \quad (1)$$

where ΔF is the resonant frequency shift of quartz crystal; F is the resonant frequency of the quartz crystal; Δm is the surface mass change; μ is the shear modulus of the quartz crystal; ρ_Q is the density of the quartz crystal and A is the surface area of the quartz crystal.

The ideal mass sensitivity of the quartz crystal can be calculated using the Eq. (1). For an AT-cut quartz crystal, where v_q=3,340 m/s, ρ_q=2,650 kg/m^3, the equation becomes a simple form.

$$\Delta f = -2.3\times10^{-6} f_0^2 \Delta m/A \quad (2)$$

Where f_0 is in MHz, Δm in g and A is active surface area in cm^2. Therefore, a 9 MHz QCM with 0.2 cm^2 surface area has a mass sensitivity about 1.1 ng for 1 Hz change in the resonant frequency.

Although the assumptions for both forming an elastic film and no radial influence of the sensitivity on the electrode are necessary to use these equations, these are believed as a suitable equation to treat the obtained frequency data of the QCM in the atmosphere condition. Though Eq. (1) shows the possibility of the quartz crystal applications in the gas phase, the possibility of the quartz crystal applications in liquids was in question.

In 1985, it was reported that it is possible for the quartz crystals to oscillate in contact with liquids. Several applications have been published, including determination of ions, immunoassays, liquid chromatography and an electrochemical application. The frequency shift of the quartz crystals in contact with liquids has been studied [74-80]. Kanazawa et al. [61] derived the following equation for ΔF from the equations of the shear stress relationship in the quartz crystal and for the liquid.

$$\Delta F = -F^{3/2}(\rho_L \eta/\pi\mu\rho_Q) \quad (3)$$

where η is viscosity of the contacted liquid and ρ_L is the density of the contacted liquid. In Eq. (3), it is understandable that the resonant frequency change of the quartz crystal includes the information of mass change and viscoelastic change of its contacted environment.

A further approach has been introduced by measuring additional parameters of the oscillating quartz crystal. For this purpose, the electrical equivalent circuit parameters are computed, and an equation for the properties of R_1 (resonant resistance) and liquid properties is derived based on the admittance measurement of the quartz crystals using an impedance analyzer. The resonant resistance of the quartz crystal is the resistance included in the electrical equivalent circuit of the quartz crystal. For the quartz crystal in contact with liquids, the resonant resistance has been founded to be [80]:

$$R_1=(2\pi F\rho_L\eta)^{1/2}A/k^2 \quad (4)$$

Where, k is the electro-mechanical coupling factor.

Using the equivalent circuit, the resonant frequency of the quartz crystal is expressed as $F=1/2\pi(C_1L_1)^{1/2}$. Here, the capacitance (C_1) reflects the elasticity, and the inductance (L_1) reflects the total mass of the quartz crystal and contact materials on it. This equation implies that the resonant frequency change includes the information of the mass change and elasticity change on the quartz crystal. The typical models on the shear vibrating quartz crystal coated with an elastic films (a), in contact with liquid (b), and coating with viscoelastic films (c), are expressed in Fig. 2 [81].

For the elastic film coated quartz crystal (Fig. 2(a)), the resonant frequency is decreased with the elastic mass loading, while the resonant resistance is not altered, since there is no vibration energy loss in the films. For contact with liquid, the resonant frequency change reflects the mass effect of the liquid that moves with the shear vibrating quartz plate. This means the surface mass effect causes a resonant frequency change dependent on the contact material characteristics. As the factor $(\rho_L\eta)^{1/2}$ appears in both Eqs. (3) and (4), the resonant frequency change and the resonant resistance have a linear relation as shown in Fig. 2(b).

Fig. 2(c) shows the qualitative explanation of the viscosity change

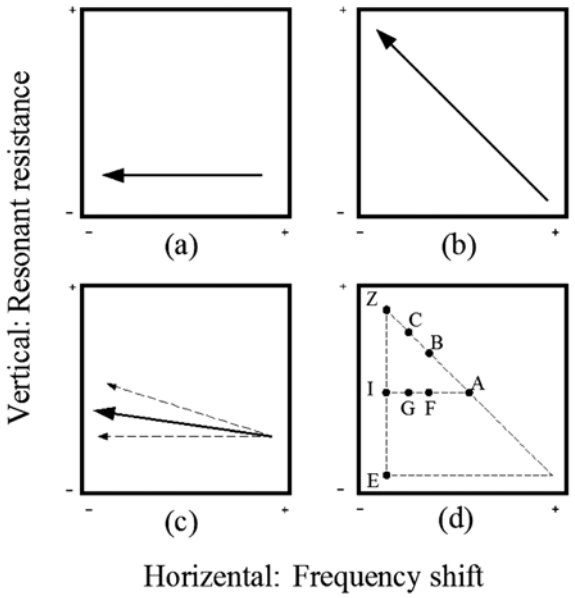

Fig. 2. Quantitative patterns on the changes of resonant frequency and resonant resistance for elastic film coating (a), viscosity change contact with water (b), viscoelastic film coating (c) and the final F-R model (d).

of the viscoelastic film coated quartz crystal. This figure is obtained as middle between Fig. 2(a) and Fig. 2(b). The same behavior is suggested by Crane's theoretical study on the viscoelastic film coated quartz crystal. In this pattern, the film thickness increases (e.g., the mass increase) with the increasing of the resonant resistance (e.g., the viscosity increase in the film). This F-R diagram is supported by the experimental results of the electrochemical deposition of polypyrrole, where the ratio between the resonant frequency and the resonant resistance changes varied with the film viscoelasticity change, which is especially changed by the swelling phenomena [65]. Summarizing these changes produces the F-R relation for various kinds of mass-bindings as shown in Fig. 2(d).

In Fig. 2(d), the change of A→B→C shows the viscosity increase in liquid films. Here, the liquid film has no elasticity and the viscous penetration depth in the films increases with the viscosity. The oscillation decay layer increase in the films causes the vibrating mass increase on the quartz crystal surface with producing the decrease of the resonant frequency. This viscosity increase also results in the resonant resistance increase. The slope for A→B→C line in this diagram is equal to that in Fig. 2(b). When the films have high viscosity, the transverse viscosity wave does not vanish within the film limiting the resonant frequency and resonant resistance changes, and point Z in Fig. 2(d) is obtained as the extreme point. The resonant frequency change at the point Z corresponds to the resonant frequency change for perfect elastic films (point E) because the resonant frequency change reflects the total vibrating mass on the quartz crystal surface. When the film elasticity increases in fluid films, the resonant frequency decreases as A→F→G→I in Fig. 2(d). In this case, the extreme point I is determined by the film thickness limit. The change E→I→Z in Fig. 2(d) shows the viscosity increase in the elastic films. This change includes the viscosity change in the films as shown by the dashed line in Fig. 2(c). The changes in Fig. 2(d) suggest that the resonant resistance reflects the viscosity change and that the resonant frequency reflects the elasticity change in a small viscosity and elasticity region. In this region, the film thickness is an important parameter which determines the extreme points of the resonant frequency and resonant resistance changes. Using the models in Fig. 2, of the rheological changes in the coating films can be explained by drawing the resonant frequency and resonant resistance changes in experiments. If two different phenomena occur simultaneously, the changes in the F-R diagram are expressed by a sum of the F-R vectors.

The resonant condition can be evaluated by analyzing the admittance measurement of a quartz crystal in experiments. The resonant frequency and the resonant resistance are determined by the admittance measurement of a quartz crystal in the electrical equivalent circuit [80]. The admittance of quartz crystal is expressed as follows:

$$Y=1/(R_1+j\omega L_1+1/j\omega C_1)+j\omega C_0 \quad (5)$$

Eq. (5) is convertible using conductance (G) and suceptance (B) as follows:

$$(G-1/(2R_1))^2+(B-\omega C_0)^2=(1/(2R_1))^2 \quad (6)$$

The resonant resistance is obtained as the reciprocal expression of the maximum conductance value. In our experiments, about 2000 measurements of admittance (G and B) were performed by the stepped

frequencies of 25 Hz in the resonant region using an impedance analyzer. The radius of circles on the admittance diagrams was determined by adopting the data in Eq. (6). The least square method was applied for these calculations. The resonant frequency was determined from the maximum conductance point on the admittance diagram. About 10 points around by these maximum points were applied to a polynomial equation, and the frequency value of this maximum was determined from the equation. In this measuring system, the frequency range was set up automatically using a resonant frequency value previous to the center frequency of the next measuring frequency range. The average measurement interval was about 30 sec at the continuous measurement. The reproducibility of this resonant frequency measurement was within 1 Hz for the quartz crystal in the air and 10 Hz for the quartz crystal immersed in the water at 30 °C.

The quality factor (Q factor) of a quartz crystal is defined as the ratio of the energy stored to the energy lost during oscillation and is nearly equivalent to the inverse of energy dissipation during oscillation [82]. As well as the resonant resistance, the Q factor is useful for characterizing the resonant properties of the quartz crystal [83]. The Q factors of the quartz crystal are also calculated by applying the following equation:

$$Q=\omega_s/(\omega_2-\omega_1)\approx\omega_{G\,max}/(\omega_2-\omega_1)$$

$$\text{Additionally, } \omega_s=\sqrt{1/LC}\text{, i.e. } \frac{1}{R}\sqrt{\frac{L}{C}} \quad (7)$$

where L is inductance; C is serial capacitance; R is the resonant resistance; ω_s is the frequency giving the maximum value of conductance G; ω_1 and ω_2 are the frequencies at the maximum and minimum values of suceptance B.

The concept of the resonant resistance is helpful for understanding the mechanism occurring on the surface of the quartz crystal. An easy method for the measurement of this parameter is to utilize an impedance analyzer but these methods cannot apply in high-speed data acquisition applications [69,70]. By a computerized programming technique, we could get measuring intervals of about 30 seconds using an impedance analyzer [69], but this relatively high speed in the impedance analyzer was still not usable in applications such as electrochemical measurements and general high speed sensing. For the purpose of the high-speed data acquisition, we introduced QCA917 (Seiko EG&G) and applied it to the electrochemical deposition of polypyrrole [65]. The measuring principle of QCA917 for resonant resistance is schematically depicted in Fig. 3.

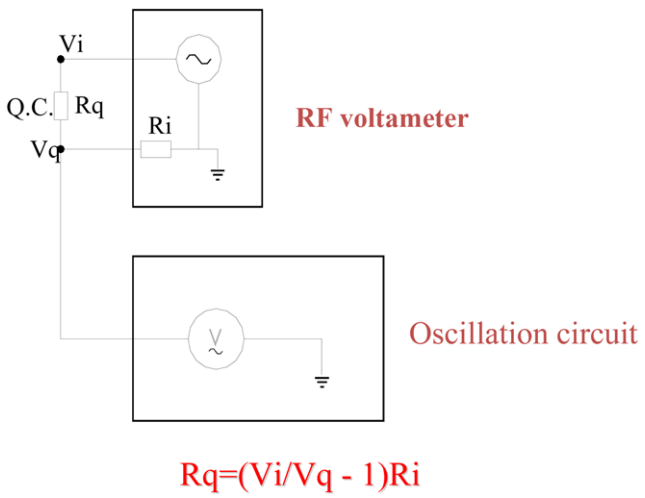

Fig. 3. The measuring principle of quartz crystal analyzer.

As shown in Fig. 3, the amplitude "Vq" , the signal of the quartz crystal terminal, is determined using the resonant resistance "Rq" of the quartz crystal and the input impedance "Ri" of the quartz crystal oscillator circuit when the AC signal amplitude "Vi" is input to the quartz crystal from the output side of the oscillator circuit. Thus, the following relation can be obtained.

$$V_q=(V_i/V_q-1)R_i \quad (8)$$

After the peak voltage of the AC signal "V_q" is converted into DC voltage, the AD-converted voltage is output as the resonant admittance intensity "V_q". "V_i" and "R_i" are almost constant but three values named as LOW, MEDIUM and HIGH. The meaning of these values is the applicable ranges. At any case, the admittance values can be converted to the resonant resistance value applying Eq. (8). For this purpose, there is a necessity for calibrating the output voltage to the resonant resistance value. Authors calibrated these three ranges and the results are plotted in Fig. 4 for the case with or without a potentiostat using glycerol/water solutions [68].

These calibrations were performed using an impedance analyzer and a QCA917 as well. Though usable ranges of QCA917 for the viewpoint of the resonant resistance are restricted in certain ranges, the calibrations show simple linear relations in all modes.

2. Applications of the Quartz Crystal to the Immunosensors

The immunoassay techniques of radioimmunoassay (RIA), flu-

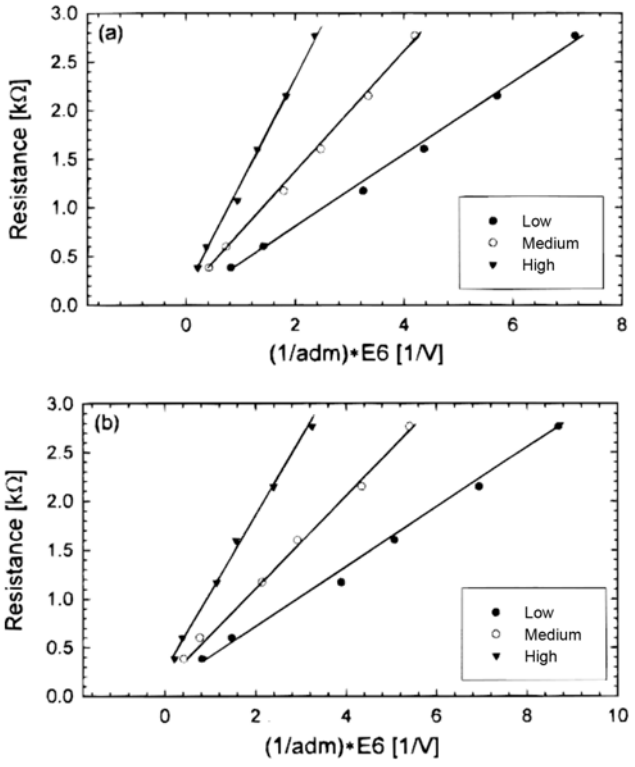

Fig. 4. The calibration of the quartz crystal analyzer with respect to without (a) and with (b) a potentiostat.

oroimmunoassay (FIA), enzyme immunoassay (EIA), and latex immunoassay have been widely applied. They still suffer, however, from the drawback of complex, time-consuming procedures and potentially hazardous or expensive materials. The piezoelectric crystal immunosensors were considered as a simpler and easier method if the crystal surface was modified with an adequate receptor to the antigen because the resonant frequency of an oscillating piezoelectric crystal could be affected by a change in mass on the crystal surface. Surface acoustic wave (SAW) devices used for micro-gravimetric immunoassay of human IgG have been reported [84], as well as AT-cut piezoelectric crystals modified with antihuman IgG, which exhibit a change in the resonant frequency on the binding to human IgG and IgG sub-classes [85]. The measurements of microbes, antigen, protein and bacteria are required for medical analyses, food analyses and bioreactor controls [86-88]. A pathogenic microbe *Candida albicans* could be detected by using a quartz crystal modified with a *Candida* antibody. Normally, the sensitivity for the bacteria such as *Escherichia coli* has not be considered as good because the cell size of the bacteria is smaller than that of *C. albicans*. Piezoelectric immuno-sensing is simpler and easier compared with other immunosensing methods, but the sensitivity of the piezoelectric immunosensing is lower than that of other methods. Therefore, the amplification of the signal has been tried. Here, we describe some piezoelectric immunosensors and amplification techniques [87].

The determination of *C. albicans* is important in clinical analyses. *C. albicans* is found in the human body even under normal conditions, but an increase in the cell population can induce infection and disease. *C. albicans* is conventionally assayed by the visual inspection of antibody-antigen (Candida species) aggregate formation. This method, however, requires a skilled technique, is time-consuming and gives only a semi-quantitative assessment of the *C. albicans* concentration. Matsuoka et al. [89] showed that a potentiometric method could be applied to a *C. albicans* immunoassay. In this method, the negatively charged *C. albicans* is adsorbed onto an antibody-bound membrane, inducing a considerable change in the membrane potential. Another immunoassay based on an electric pulse technique was also proposed and applied to the *C. albicans* immunoassay [90]. Although the piezoelectric immunosensor is not as sensitive as the potentiometric method, it has greater advantages in both its convenience of use and its wider effective concentration range. Improvement in the techniques used for the antibody immobilization may enhance the sensitivity of the piezoelectric sensor.

The antibody immobilization on the surface of the quartz crystal was achieved as follows. Silver electrodes were formed on the crystal by a vacuum deposition method and were plated with palladium. The palladium electrodes were treated by an anodic oxidation technique. The silver electrodes were also coated with silicon dioxide by a sputtering technique. Then the electrodes were treated with γ-aminopropyl-triethoxysilane (γ-APTES) (2% in acetone) for 1 hr at 25 °C. After air-drying, the electrodes were placed in aqueous glutaraldehyde (5%, pH 7.0) for 3 hr or acetone containing pyridine (1.2%) and tresyl chloride (5%) for 30 min [91]. After these treatments, *Candida* antibody (10 mg/ml), protein A (1 mg/ml), or antiserum of anti-*E. coli* was immobilized onto the surface. After the immobilization (1 hr), the remaining active sites were blocked by stirring with 0.1 M glycine solution. To improve the sensitivity of the *E. coli* detection, the resonant frequency shift was increased by further treatment to bind micro-particles modified with *anti-E. coli*. Antiserum of 1 ml anti-*E. coli* and the suspension of the particles 1 ml were mixed. Anti-*E. coli* was immobilized onto the surface of the particles by stirring the mixture for 1 hr. The particles were washed with phosphate butter (pH=7). The modified piezoelectric crystals were dipped in the microbial suspension for 30 min to allow the antigen-antibody reaction between the immobilized antibodies and the microbes. The quartz crystals were then rinsed with 0.5 M NaCl and water, dried in air and the resonance frequency change was measured. For the monitoring of IgG, the protein A immobilized piezoelectric crystal was placed inside a flow cell. The cell was rinsed with glycine-HCl buffer (pH 2.4, 0.1 M) to remove any adsorbed material, and then washed with deionized/distilled water. The resonance frequency was then monitored at a constant flow rate (0.7 ml/min) at 30 °C. The steady resonance frequency (F_1) was obtained after 5-10 min. The water was drained off and the human IgG solution in the phosphate buffer was injected into the experimental cell. After incubation (30 min), the crystal was rinsed with 0.5 M NaCl solution to remove any nonspecifically adsorbed IgG and the resonance frequency (F_2) was measured again in the flowing deionized/distilled water. IgG bound to protein A was removed with glycine-HCl buffer (pH 2.4, 0.1 M), allowing successive measurements of human IgG. Human albumin solution was also examined by the same procedure.

Fig. 5 shows the relation between the *C. albicans* concentration and the resonance frequency shift resulting from the binding of *C. albicans* in the range of 1×10^6-5×10^8 cells/cm^3. The resonance frequency shift in Fig. 5 also includes the frequency shift caused by the immobilization of the antibody and a little non-specific adsorption. The sensor showed no response with microbes from another yeast species (*Saccharomyces cerevisiae*). The correlation between the concentration of the suspended microbes (C_s, cells/cm^3) and the number of microbes bound (N_b, cells/cm^2) on the electrode, measured by an optical microscopic technique, was given as a linear curve of log (N_b)=0.68 log (C_s)+1.33, r^2=0.954. These results indicate that the magnitude of ΔF was related to the actual number of the adsorbed microbes.

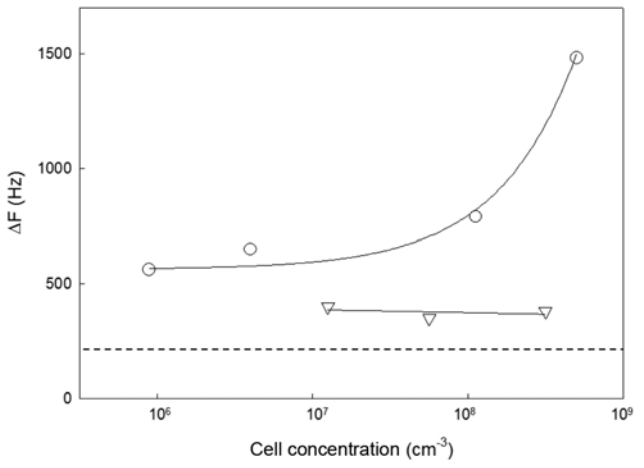

Fig. 5. The relation between the cell concentration and the resonance frequency shift (30-min reaction time) for *C. albzcans* (○) and *S. cerevisiae* (◇) The dashed line indicates the contribution of frequency shift for the immobilized antibody.

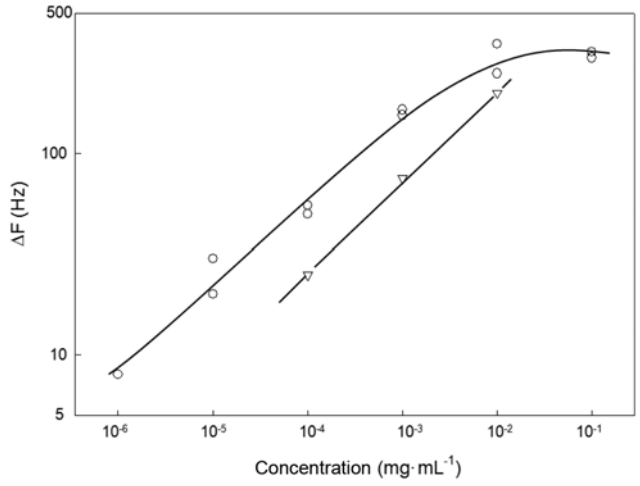

Fig. 6. Correlation between human IgG and steady resonance frequency shift for reaction time of 30 min (○) and 15 min (□).

As a similar application, the relation between the human IgG concentration and the resonance frequency shift is shown in Fig. 6. A frequency shift was influenced only by the human IgG concentration and no response was obtained for the addition of a human albumin sample solution. In the case of a 30 min reaction time, a linear correlation was obtained in the range of 10^{-6}-10^{-3} mg/ml. The resonance frequency leveled off gradually for the human IgG concentration above 10^{-3} mg/ml. The reason for this result is the binding limit of the immobilized protein A. In the case of a 15 min reaction time, a linear correlation was obtained in the range of 10^{-4}-10^{-2} mg/ml. Consequently, the human IgG concentration in the range of 10^{-6}-10^{-2} mg/ml can be determined by the system. An immobilization method using tresyl chloride has been also used to determine IgG concentration. The resonance frequency shift obtained using a 10^{-2} mg/ml IgG sample solution for 30 min of the reaction time was from 191 to 165 Hz. The frequency shift values obtained by tresyl chloride were similar to those obtained by using the γ-APTES method. It seems reasonable to assume, therefore, that the two immobilizing methods give enough active sites to bind the protein, and that the protein A is closely packed on the surface of the crystal.

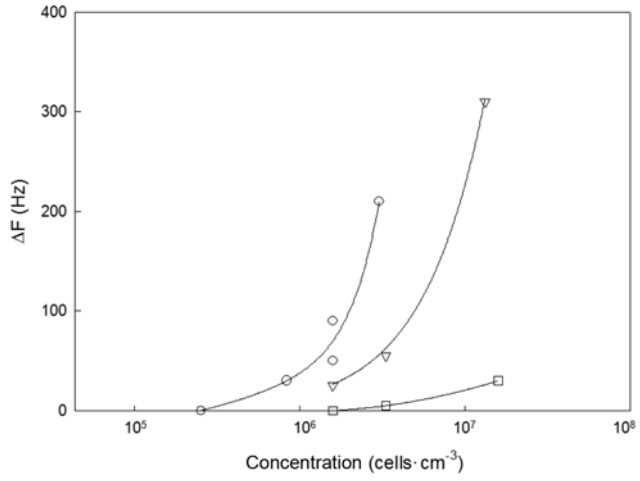

Fig. 7. Correlation between *E. coli* concentration and resonance frequency shift with the additions of polystyrene particles of 1 μm (○) and 0.5 μm (△) and without the treatment (□).

Fig. 7 shows the resonant frequency shifts for dipping in *E. coli* suspensions with treatment with 0.5 μm and 1 μm *E. coli* antibody modified polystyrene particles in comparison with the result before the treatment. Fig. 7 shows that the treatment with the polystyrene particles increased the resonant frequency shift and that the detection limit has been improved to 10^5 cells/cm^3 by the use of the 1 μm polystyrene particles.

3. Applications of the Quartz Crystal to Gelation Detecting Sensors

A piezoelectric crystal is additionally known to be a device that can measure the liquid viscosity. Based on this fact, the sensor system has been applied to determine an endotoxin (lipopolysaccharide: LPS) concentration [63] and fibrinogen concentrations [64,92,93] using the gelling reaction with Limulus amebocyte lysate (LAL) or gelation reaction of blood. The gelling reaction is possible to apply for the detection of bacteria, when the bacteria are marked by LPS. This technique will be studied in future applications.

Endotoxin is produced by microbes and is widely found in water samples. Endotoxin is a pyrogen that constitutes the outer membrane of gram-negative bacteria. It consists of a lipopolysaccaride that includes the lipid 'A' molecule. Endotoxin assays are important for the quality control of biological products, blood products, vaccines, and other parent drugs for clinical use because the injection of endotoxin into a human body can increase body temperature and induce endotoxin shock. The core basis for the endotoxin assay is the fact that the horseshoe crab blood coagulates when the bacterial endotoxin is added to it [94,95]. LAL has been purified from the horseshoe crab blood, and the gelation process of LAL has been shown to be an enzymatic cascade reaction [96]. This gelation reaction has been used to determine endotoxin concentrations based on the "LAL test". In a typical LAL test, the LAL reagent and sample endotoxin solutions are mixed in a test tube and incubated at 37 °C for 1 hr. The gel formation is scored visually to indicate an endotoxin concentration [95]. This in vitro method is more quantitative and economical than the *in vivo* method in which a sample is injected into a rabbit and the increase in the body temperature is measured. An apparatus that measures turbid metric kinetics allows one to determine the endotoxin concentration in a simple operation [97,98]. On the other hand, the quartz chemical analyzer (QCA) is a useful and sensitive device for the direct endotoxin determination [63]. QCA measures changes in sample viscosity of an interfacial thin layer on the quartz crystal surface, requires a small quantity of the sample and LAL reagent, and can also analyze turbid samples.

Endotoxin sample solutions were prepared by diluting the standard endotoxin. The sample solution (0.2 ml) was incubated at 37 °C and added to a lyophilized LAL solution. The mixture was poured into a well-type experimental cell, and the resonant responses of the modified quartz crystal were measured using an impedance analyzer or a QCA 917 instrument after incubation at 37 °C. In the case of the fibrinogen determination, fibrinogen sample solutions were prepared by diluting the standard solution to 500, 250, 125, 50 and 0 mg/dl. First, 0.2 ml of a fibrinogen sample solution was incubated at 37 °C and injected into a liquid cell, which was also incu-

bated at 37 ℃. The thrombin solution (0.2 ml, 20 ℃) was then added and mixed quickly. The resonant frequency was measured with a gate time of 0.1 s and an accuracy of 10 Hz. The frequency data were stored and manipulated in a computer, which requires 152 ms for each frequency measurement.

Fig. 8 shows the response change of the resonant resistance and the resonant frequency with the different endotoxin concentrations. The smaller values were obtained at higher concentrations of endotoxin as shown in Fig. 8. The result means that these changes are not only induced by the viscosity change of the liquid on gelation. A thin film, which could not be removed by rinsing with distilled water but removed with 0.1 M hydrochloric acid, was observed on the quartz crystal surface after the measurement. The thin film gave residual R and F changes. It seems that the film was produced by the adsorption of a substance included in LAL. The detection limits obtained by the measurement of R and F changes were 10 and 100

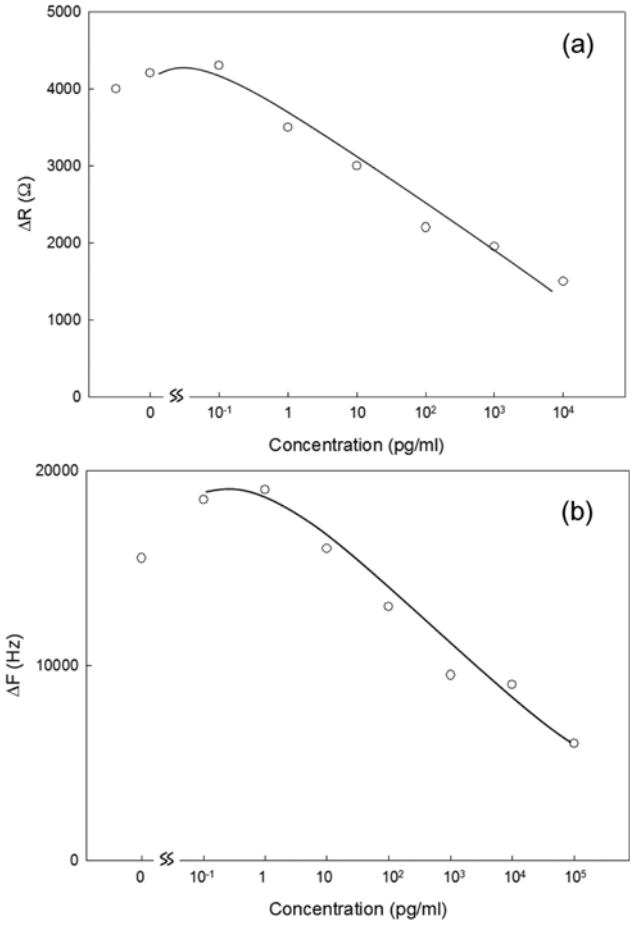

Fig. 8. Relation between endotoxin concentration and the change in resonant resistance (a) and the change in resonance frequency (b).

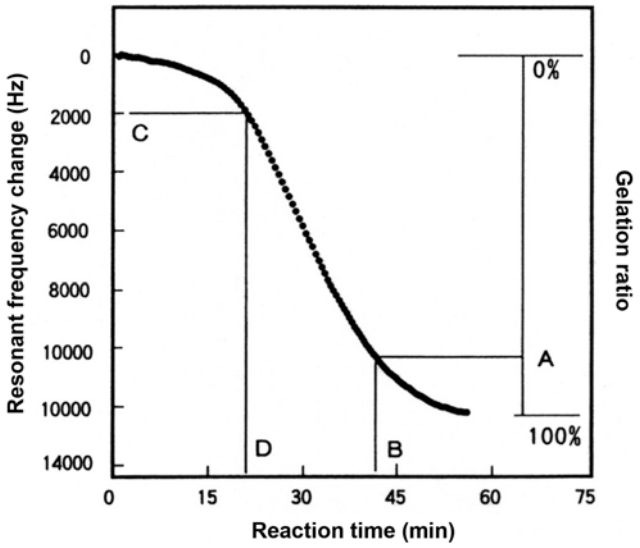

Fig. 9. Resonant frequency response to the gelation reaction of LAL regent caused by 0.025 EU/ml of a standard endotoxin. 'A' is the 90% gelation step, 'B' is the 90% gelation time, 'C' is the 2,000 Hz threshold frequency and 'D' is the 2,000 Hz threshold time.

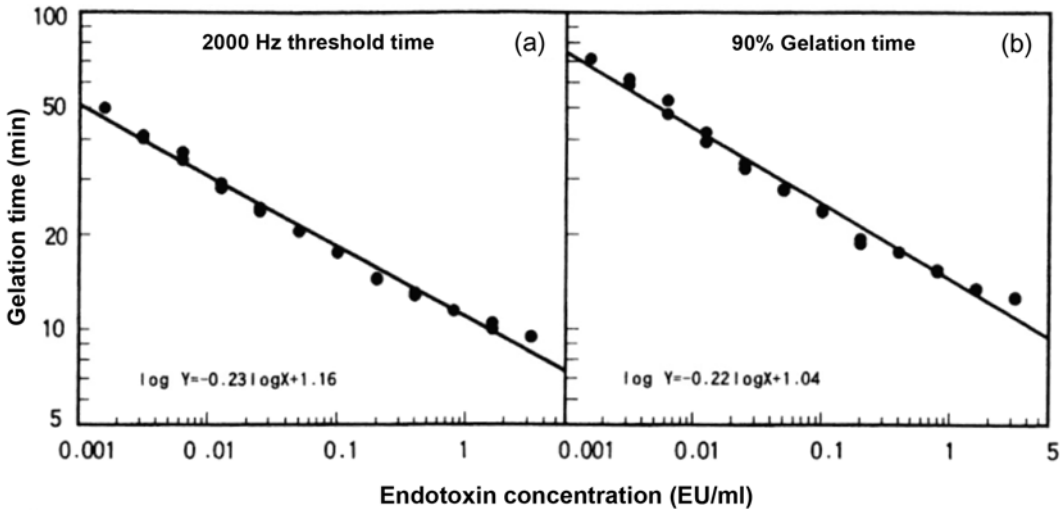

Fig. 10. Calibration curves for the endotoxin concentration vs. the 2,000 Hz threshold time and for the endotoxin concentration vs. the 90% gelation time.

pg/ml, respectively. Both the parameters have a linear correlation to the endotoxin concentrations. Although the long gelation time gives a lower detection limit, the R and F indices are better for determination of the high concentrations of endotoxin.

For faster endotoxin measurement, the gelation mechanism was studied by the quartz crystal. Fig. 9 shows the typical resonant frequency change obtained by QCA during the gelation reaction of a standard 0.025 EU/ml endotoxin solution. Gelation time was determined from the time required to reach 90% of total resonant frequency change--called the 90% gelation time. To shorten the measuring time, the threshold time was also adopted by measuring the time required to reach the threshold frequency change, 2,000 Hz (the 2,000-Hz threshold time). The 90% gelation time and the 2,000-Hz threshold time were selected for the endotoxin determination indexes after considering the data reproducibility, and the details of this selection have been explained in our previous paper [92].

Fig. 10 shows the 2,000-Hz threshold time and the 90% gelation time determined by QCA for differently diluted endotoxin solutions in distilled water. In Fig. 10, the relationship between the endotoxin concentration and the gelation time is linear for both the 2,000-Hz threshold time and the 90% gelation time over a range of 0.001-3 EU/ml (0.13-375 pg/ml) presented in double logarithmic scale. The 95% confidence interval was ±0.4 min on the 2,000-Hz threshold time and ±0.8 min on the 90% gelation time.

Fig. 11 shows the correlation between the 2,000-Hz threshold time and the 90% gelation time. This result confirms that both the 2,000-Hz threshold time and the 90% gelation time can be used for endotoxin determination. The 2,000-Hz threshold time was adopted in the following experiments to shorten the measuring time, and it is called the gelation time since it represents the same kinetics.

In this section, we describe a method for endotoxin determination by QCA and propose that QCA may be applicable to many other assay systems. For example, factors in blood coagulation (fibrinogen, factor IIX, IX, etc.) and anticoagulants (ATIII, etc.) could be

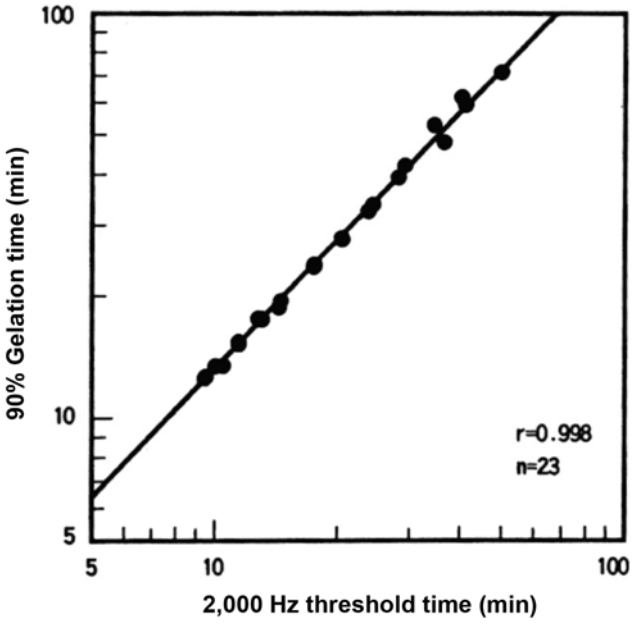

Fig. 11. Correlation between the 2,000 Hz threshold time and the 90% gelation time.

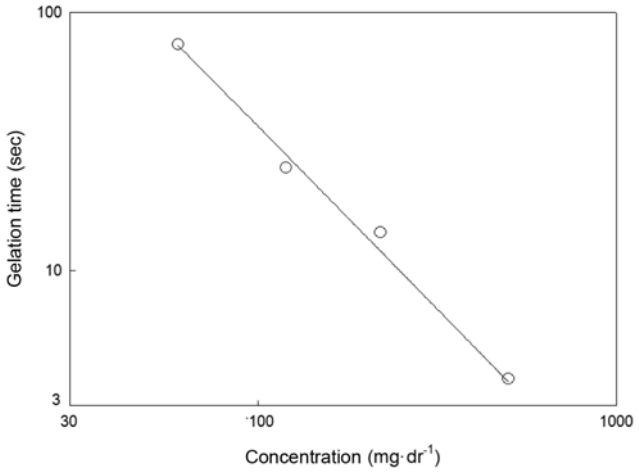

Fig. 12. Relation between fibrinogen concentration and gelation time using aluminum oxide particles.

assayed in human blood using the QCA method [88,92].

As a similar application, the gelation of fibrinogen was also measured as shown in Fig. 12. The relation between the fibrinogen concentration and the gelation time (Fig. 12) shows a good linearity and a good agreement with the results of conventional methods.

4. Extension of the Quartz Crystal Application Coupled with Other Apparatus

The applications of the piezoelectric crystals were extended to the determination of thin layer thickness and the analysis of the microrheology of liquid crystals and electrochemically polymerized thin films. Several research groups have already tested different combinations of receptors and transducers. Yet, the selectivity and sensitivity are not enough and the reliability is questionable, as the sensing signal is usually only obtained based on one analytical variable. Therefore, new attempts have also been made to develop sensing systems that obtain multiple sets of analytical variables simultaneously.

We also studied the simultaneous sensing systems to analyze the viscoelastic characteristics of polymer blend thin films using quartz crystal resonance (QCR) and differential scanning calorimetry (DSC), the local viscoelasticity simultaneous with the surface morphology of polystyrene thin films using the QCR and atomic force microscopy (AFM), the electrochromic and viscoelastic property changes of polypyrrole thin films during the redox process using the QCR and UV-Visible Spectroscopy, the capacitor characteristics and surface morphology of polymer thin films using the QCR and AFM, the morphology and physical properties of cultured cells using a micro camera and the quartz crystal, and the simultaneous SPR and QCM sensing system. In this review, we describe the applicability of the quartz crystal combined with a CCD camera to illustrate the performance and the future possibilities of quartz crystal sensors. A QCM system with a micro CCD camera, which can observe the cell structure changes with CCD camera and measure the viscoelastic characteristics of the cell with the QCM measurement simultaneously, was developed to investigate the effects of chemical stressors on the cultured cells. Understanding the characteristics of the cultured cells for both the viscoelastic characteristics of the cultured cell and the cell shape is important because both of them are important factors for the cell activity [99,100] and the cell adhesive

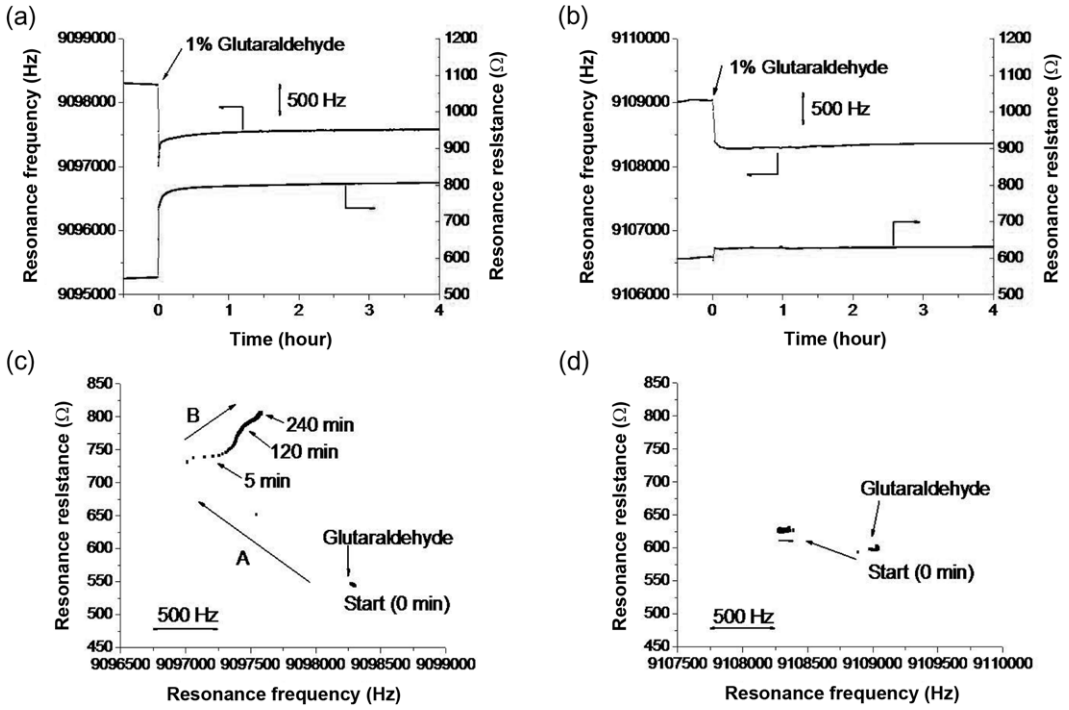

Fig. 13. QCM measurement results for 1% GA treatment. Time course of the resonance frequency and the resonance resistance (a), (b) and (c), (b) F-R diagram replotted from (a) and (b) with HepG2 cell seeded (a), (c) and without seeded (b), (d).

function [101,102]. The viscoelastic characteristics of the cultured cell could be analyzed using the resonant frequency and resonant resistance diagram. The resonance frequency and the resonance resistance were measured by using the QCA922 (Seiko EG&G, Japan). A quartz crystal sensor was sandwiched between the culturing chamber and the sensor holder. A white LED was used as a light source. A micro CCD camera (Plumnet, Japan) was mounted on the sensor holder. Since the culturing chamber containing the micro CCD camera was put into the incubator, it is necessary to move the culturing chamber for microscopic measurements. In this application, a glutaraldehyde (GA) [103] and a t-butylhydroperoxide (t-BHP) [104, 105] were used as chemical stressors.

Fig. 13 shows the resonant frequency and resonant resistance changes of the cultured HepG2 cells treated with 1% glutaraldehyde. Fig. 13(a) is the resonance frequency and the resonance resistance responses when glutaraldehyde was injected into the cell cultured chamber where the cells were cultured at least 12 hrs. Fig. 13(b) is the result of the blank experiment in which the cell was not seeded. The corresponding time-based CCD images are available in original papers [106,107]. The changes of the resonance frequency and the resonance resistance by the collagen film loading without the cultured cell (Fig. 13(b)) are smaller than those of the cultured cells (Fig. 13(a)); and the resonant frequency of the collagen film modified quartz crystal without cultured cell is reached to a steady state after a few minutes, while that of the cultured cells is decreased initially and increased continuously after then. The cross-linking reaction of glutaraldehyde at the surface of the collagen film could cause a resonant frequency decrease and resonant resistance increase. On the contrary, the covalent bond forming between amine groups of the proteins by a glutaraldehyde could cause a resonant frequency decrease and a resonant resistance increase initially, but the structure change of the cultured cell could cause a resonant frequency increase continuously. This was additionally confirmable from the CCD images [106,107].

To understand these phenomena, the F-R diagrams and the microphotographical changes after injecting glutaraldehyde were compared as shown in Fig. 13(c) and Fig. 13(d). Even though only little changes in the cell shape were shown [108], a small shrinkage in the cell size could be observed in the CCD images. At the initial stage of the glutaraldehyde injection, the cross-linking reaction of membrane proteins caused the fluidity of the cell membrane decreasing and elastic property increasing. After then, the shrinkage in the cell size by the glutaraldehyde caused the viscous property increment and the mass effect decrement. The F-R diagram of the Fig. 13(c) could be divided into two parts. In part 'A', the resonance frequency was decreased and the resonance resistance was increased in the initial step, which implies a viscous property increase on the quartz crystal. In the next step 'B', the resonance frequency was increased with the increase of the resonant resistance, which meant an increased viscous property and a decrement in the mass effect; thus, it corresponds to the rigidity decrease of the loading material on the quartz crystal. It is supposed that the cross-linking reaction increased the viscous property of the HepG2 cells; on the contrary, the shrinkage in the morphology was related to the rigidity. These results represented the applicability of the QCM measurements coupled with the CCD camera to the evaluation of the cell activities.

NANO-DIAGNOSIS METHODS USING AFM

The scanning tunnel microscope (STM) measures the tunneling currents by bringing the metal probe close to a conductive sample surface at the interval of 10 Å or less using the well-known tunnel-

ing effect. When scanning with the sharp probe end close to the surface of the sample is performed, the current change takes place based on the unevenness of the sample surface due to the tunneling effect. At this point, a three-dimensional surface image can be obtained. If the probe is carefully controlled to avoid the contact of the sample surface using piezoelectric element, the surface morphology of the atomic level can be measured. If the feedback control is based on the atomic level interaction, the instrument is called an atomic force microscope (AFM). In this case, it enables measurements in liquid as well as in air unlike the conventional electron microscopes. Although STM has a limitation of observing only the conductive sample surface, the AFM enables the observation of insulating materials unlike the STM.

Compared to the scanning electron microscope (SEM) or transmission electron microscope (TEM) that observes samples using electronic waves or beams, scanning probe microscopy (SPM) including STM and AFM is based on various physical interactions between the sample and the probe such as repulsive force, attractive force and magnetic force acting between atoms. The basic principles of SPM that detects various physical interactions acting between the probe or the cantilever and the sample surface are described in Fig. 14.

There are normally two measuring parameters based on the change in the small cantilever. The first is measuring physical interactions and the second is measuring the displacement of a beam reflecting angle at the rear of the lever. When scanning the probe on the surface is performed, the corresponding force such as tunnel currents, repulsive force, attractive force, magnetic force, electric force, friction force, and adhesive force can be measured as the physical interaction, whereas the morphological structure of the sample surface is interpreted by measuring the reflected beam angle change in the cantilever [108,109]. In addition to the surface observation of metals or semiconductors, these scanning probe microscopes are reported to be widely applied to the absorbed state of organic molecules [110], LB film [111], liquid crystal [112], and biological substances such as DNA [113,114], proteins [115,116], cell membranes [117,118], lipid bilayer [119,120], and antibodies [121,122].

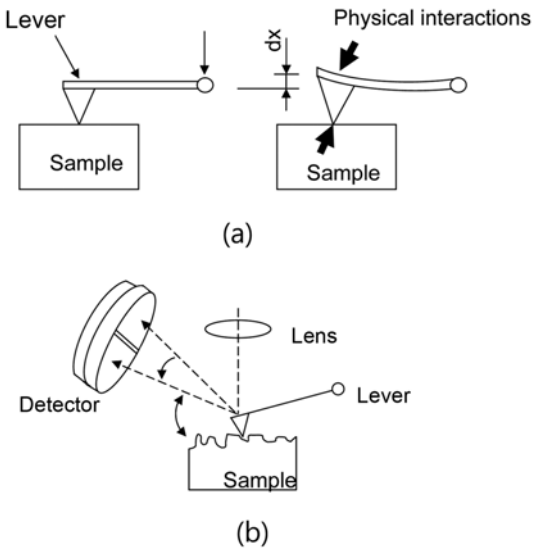

Fig. 14. The schematic diagrams of the AFM principle for the tip-sample interaction (a) and optical-beam reflection measurement (b).

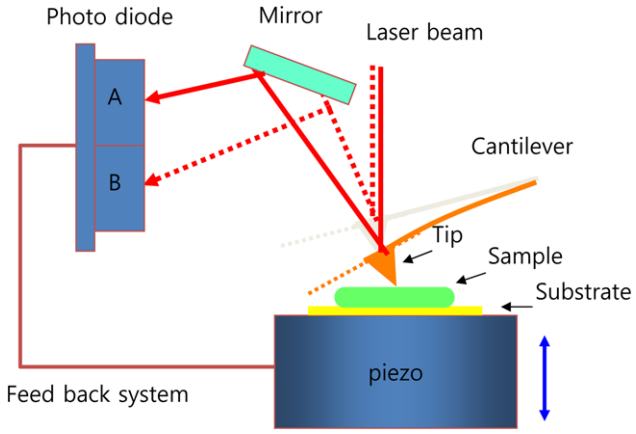

Fig. 15. The feedback system of AFM measurement.

In recent years, researches on the application of AFM and the nano-probe to the manipulation technology of low-invasive single cell and high efficient gene delivery technology have been actively conducted [123-131]. Cell manipulation is important in biotechnology. In particular, the technology of gene delivery into living cells has a potential to be developed as a base technology not only in cell biology but also for new future medicine.

In the current review, the results of nano-diagnosis using AFM, and the manipulation technology of low-invasive single cell and high efficient gene delivery technology using the nano-probe and atomic force microscopy will be briefly introduced.

1. Principle of the Nano-diagnosis Based on the AFM

As shown in Fig. 15, a typical AFM system consists of a microfabricated cantilever probe, a piezoelectric (PZT) actuator; a position-sensitive photo detector for receiving a laser beam reflected off the end-point of the cantilever provides a cantilever deflection feedback [132]. The principle of AFM operation is to scan the tip over the sample surface with feedback mechanisms that enable the PZT scanners to maintain the tip at a constant force, or constant height above the sample surface. As the tip scans the surface of the sample, moving up and down with the contour of the surface, the laser beam deflected from the cantilever provides measurements of the difference in light intensities between the upper and lower photo detectors. The feedback signal based on the different photodiode signal by X-Y location, through software control from the computer, enables the tip to maintain either a constant force or constant height above the sample. In the constant force mode, the PZT transducer monitors a real-time height deviation. In the constant height mode, the deflection force on the sample is recorded.

In addition to topographic measurements, the AFM can also provide much more information and applications. Another major application of AFM is a force curve measurement, the direct measurement of tip-sample interaction forces as a function of the distance between the tip and a sample in the approach and retraction parts. Fig. 16 shows a schematic diagram of the movement of the cantilever and tip during the force spectroscopy measurement. The measurement has been used to measure nanoscale contacts, atomic bonding, Van der Waals forces, and Casimir forces, dissolution forces

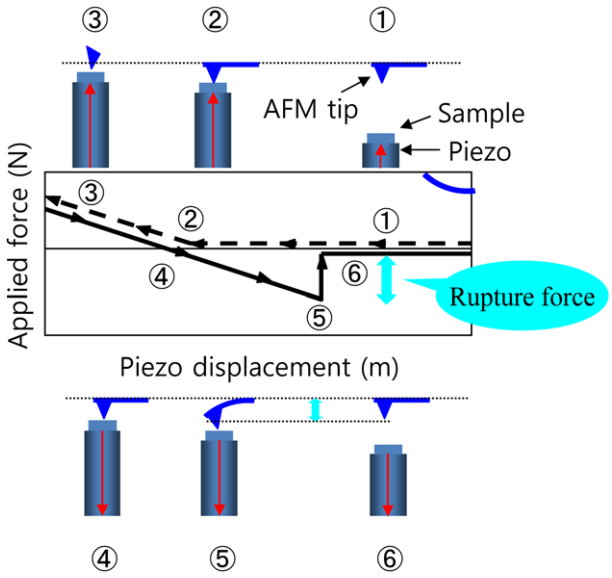

Fig. 16. The principle of AFM force curve measurement and the location of the tip.

in liquids and single molecule stretching and rupture forces. The AFM force spectroscopy allows the measurement of pico-netwon (10^{12} N) forces associated with single molecules, thereby providing fundamental insights into the molecular basis of biological phenomena as diverse as molecular recognition, protein folding and unfolding, DNA mechanics and cell adhesion [133]. The force microscopy has been applied in many biological areas, such as antigen-antibody pairs, protein-ligand interactions, protein-membrane interactions, and protein-cell interactions. A detailed review of these applications can be found in a few excellent reviews available elsewhere [134,135]. Recently, a nanoscale surgical operation of a living cell using an AFM with a nanoneedle has been researched intensively by Han et al. [123-131].

Fig. 17 shows a fabricated nanoneedle and a schematic illustration of a gene delivery system using the nanoneedle. The nanoneedles were prepared using a focused ion beam etched from pyramidal Si AFM tips that had spring constants of approximately 0.2 N/m. The GFP or DNA adsorbed nanoneedle was inserted into the human MSC with simultaneous monitoring of the applied force on the cantilever. The DNA-adsorbed nanoneedle remains inserted for a few minutes to diffuse the DNA from the surface of the needle to the nucleus, and is then evacuated from the cell. By applying this, the gene delivery of specific purpose was possible without any damage of the cells [128].

Due to its inherent advantages, AFM's find a variety of applications that range from nanofabrication to biological materials [136-146]. We classify the diverse applications of AFM into two major categories: molecular metrology and biological sciences. The former category mainly deals with engineering applications that span over various manufacturing fields, such as testing of electronics components and fabrication of miniature mechanical parts. The latter category deals with the implementation of AFM in crucial biological applications to determine cell/cell or cell/protein interactions and to observe cell movements in living species. The ability of AFM to measure forces in the sub-nN range under physiological conditions makes it an attractive tool for studying many biological applications such as drug/protein interactions, protein/protein interaction, cell/cell or cell/protein interactions and many other largely intermolecular forces governed phenomena. Specifically, the quantification of these molecular interactions in biological systems is of interest to many researchers and engineers. A molecular level understanding of the interfacial adhesion is a necessary part of unraveling these phenomena and would be of tremendous potential benefit in associated applications such as rational drug design, molecular electronics, biomaterials development, or biosensor design. Based on the AFM's ability to generate topographical images, the AFM has evolved into a useful tool for probing single molecules. High lateral resolution (<1 Å) and the ability to detect low interaction forces (<1 pN), along with the ability to operate under aqueous or physiological conditions makes it a good technique for studying biological systems. The NC-AFM can measure the topography, surface forces, and mechanical properties of a surface at the nanometer scale; furthermore, the development of chemically specific probes provides a direct tool for studying intermolecular forces [147,148]. The several applications of AFM in biological sciences are described below.

2. Characterization of Biological Material and Evaluation of the Binding Affinity of Peptide Probes to Proteins

Recently, a few groups have developed label-free DNA chips

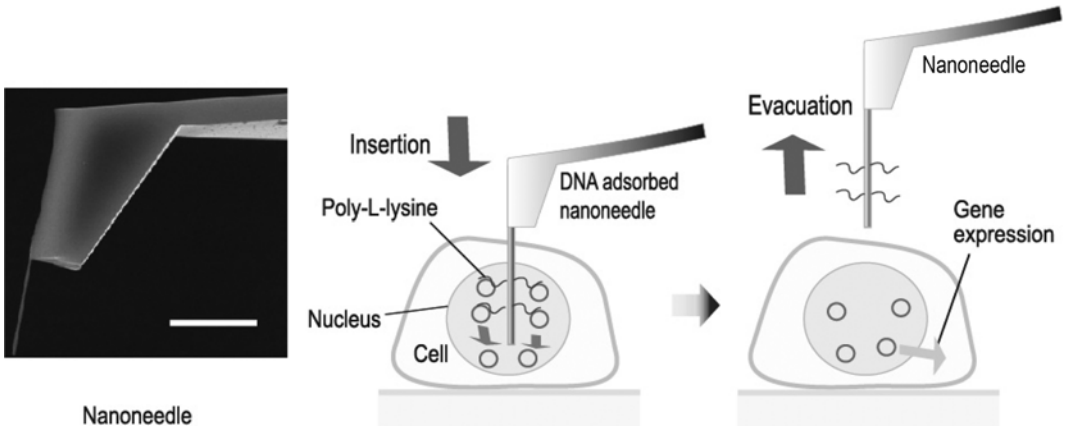

Fig. 17. The fabricated nanoneedle and schematic illustration of gene delievery using the DNA-adsorbed nanoneedle.

using protein-DNA complexes [149,150]. The chips were analyzed by using quartz crystal microbalance (QCM) [151,152] or electrochemical methods [153]. In AFM methods, direct confirmation or visualization of hybridized short oligonucleotides on a specific surface is normally difficult. The location of DNA or oligonucleotide molecules is normally on a viscoelastic surface, which produces oscillation damping of the AFM cantilever by tip adsorption on the surface. For that reason, only protein surfaces are normally obtainable with a conventional AFM method.

Phase lag imaging is a tapping mode imaging technique that shows the phase difference between driving oscillation of the piezoelectric oscillator and oscillation of the cantilevers as it interacts with the sample surface [154-158]. In a general sense, by mapping the phase lag, phase imaging surpasses simple topographical mapping to detect variations in composition, adhesion, friction, and viscoelasticity. Phase lag represents the adhesion difference between the tip and the substrate surface. In many samples, large adhesion differences are caused by differences in the thickness of the adsorbed water layer, which is a function of hydrophobicity and hydrophilicity. Possible applications include the identification of contaminants, the mapping of different components in composite materials, and differentiating regions of high and low surface adhesion or surface hardness.

A possible characterization method of originally characterizing difficult biological material was suggested by combining phase lag mapping and surface humidity control [137]. Proteins display a wide variety of biological activities. Elucidation of the interaction of proteins at the atomic level can lead to advancements in areas such as those concerned with curative diseases and the development of new medicines. A variety of methods have been reported for the evaluation of protein-protein interactions including the use of electrophoresis, two hybrid methods, the enzyme-linked immunosorbent assay (ELISA), and the fluorescence resonance energy transfer (FRET) method. These methods represent versatile techniques that have been widely used in the evaluation of protein affinity [159,160]. AFM has been used as an advanced method for the evaluation of affinity under *in vitro* conditions. Although the application of peptide probes has already been reported in the analysis of protein-protein interactions using electrophoresis, surface plasmon resonance, and quartz crystal microbalance, only a few reports have dealt with the use of force curve measurements [161,162]. The evaluation possibility of protein affinity by measuring force curves using a peptide probes was suggested by Muramatsu et al. [163].

Preparation of a gold substrate for the AFM phase mapping was reported in a previous study [164]. In a humidity-controlled experiment (we changed the sample humidity to reveal DNA oligonucleotides), the sample was located in a self-made highly humid incubator, which can control the humidity and the temperature. The relative humidity of the incubator was more than 90% at a constant temperature of 20 °C; the sample was incubated for a week. Thereby, the sample surface maintained its high humidity. The incubator was filled by dry nitrogen gas, which ensured DNase and protease free conditions. Simultaneous tapping mode topographic and phase lag imaging was carried out using a commercially available multi-functional probe station (SPI 3800; Seiko Instruments, Inc.). A normal tapping-mode silicon cantilever (spring constant 40 N/m, oscillation frequency 340 kHz) was used for imaging.

For the affinity force measurement, peptide probes H-A3GP5GP5GP5GOH (**1**), H-A3GP5G-OH (**2**), H-A3G7-OH (**3**), and H-A3G-OH (**4**) were synthesized by the solid-phase method, and carried out with a PSSM-8 peptide synthesizer (Shimadzu). Applied peptide probes were covalently immobilized on the cantilever tips. Profilin was covalently immobilized on a mica surface using a previously reported procedure [165]. The immobilization of the peptide probe on the tips was characterized by FTIR spectroscopy and XPS, and that of profilin on the mica surface was confirmed by the measurement of AFM topographic images. The spring constant of the cantilever was calibrated using the well-known thermal vibration method [166].

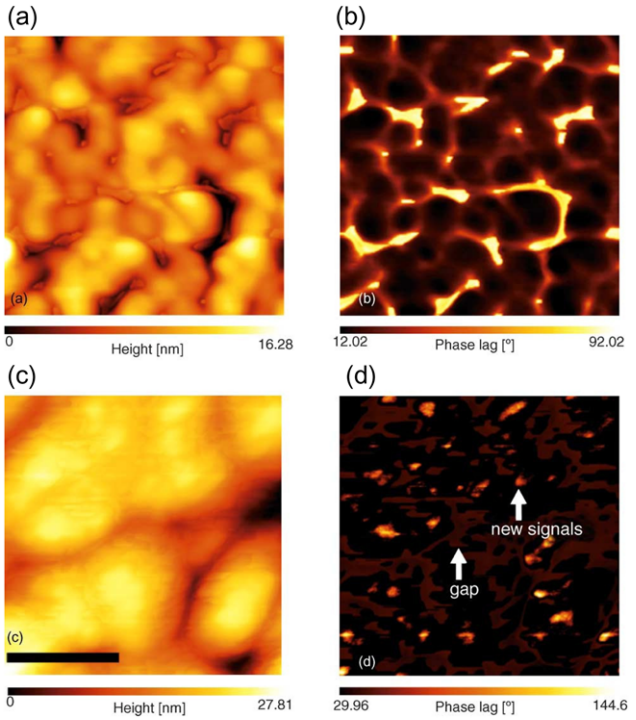

Fig. 18. AFM images of only SAv-biotin ((a) and (b)) and SAv-biotinylated DNA oligonucleotide complexes ((c) and (d)) after surface humidity control in 250 nm×250 nm scan areas. In (d), a strong new signal is observed apart from the signals of the gaps. The scale bar indicates 100 nm.

Fig. 18 shows AFM images of the humidity controlled surface for only SAv-biotin ((a) and (b)) and SAv-DNA oligonucleotide complexes ((c) and (d)). In a normal condition, such as a DNA molecule immobilized mica surface, the phase lag of the DNA showed about 10° of the phase lag value because of its hydrophilic property [156]. In the case of the SAv-biotin only surface, any difference with the originally prepared sample was not confirmable, as shown in Fig. 18(a) and (b). When DNA oligonucleotide was combined with the SAv, the humid environment had an influence on the obtained topographic and phase lag images. Topographic images composed only of SAv-biotin were relatively clearly obtained after the same humidity control (Fig. 18(a)). Therefore, the unclear topographic image could be an influence of the immobilized DNA oligonucleotides (c). Newly strong signals ranging 70-100° were obtained in the phase lag image (d). The strong signals were not from the amplified signals for the gaps between the individual SAv molecules, but from the center of the SAv molecules, as shown in Fig. 18(c)

and (d). The signals from the gaps still remained, as indicated in Fig. 18(b). The number of the localized strong signals (stronger than 70°) was about 66, which was slightly smaller than the number of the SAv molecules (approximately 70 molecules in 250 nm×250 nm with the local difference of 20%). These strong phase lag signals could not be confirmed from the sample composed only of SAv or SAv-biotin complexes after humidity control. Lee and Fritsche demonstrated the binding ratio determination of biotin on a protein done by capillary gel electrophoresis of monomeric avidin [167]. Avidin has a slightly higher affinity (Ka ca. 10^{15} M^{-1}) to biotin than that of SAv (Ka ca. 10^{13} M^{-1}) [168]. Although avidin has four possible reaction sites with biotin [169], the best experimental result shows a ratio of 1 (avidin): 2.89 (biotin) in an extremely high biotin concentration [167]. In addition, Caruso et al. reported that the interaction SAv to biotin-DNA has a maximum ratio of 1 : 2 for a 30-mer DNA oligonucleotide [151]. In our experiment, one or two reaction sites landed on the gold surface through a peptide bond. Therefore, two or three reaction sites could interact with biotin. In the biotin-DNA immobilization, electrostatic repulsion force between the DNA oligonucleotides may engender its role as an inhibitor for the binding interaction. In addition, the AFM effective tip size [170] is slightly larger to resolve neighboring individual DNA oligonucleotides. Considering the SAv geometry, sub-5 nm AFM tip size was strongly required to resolve clearly.

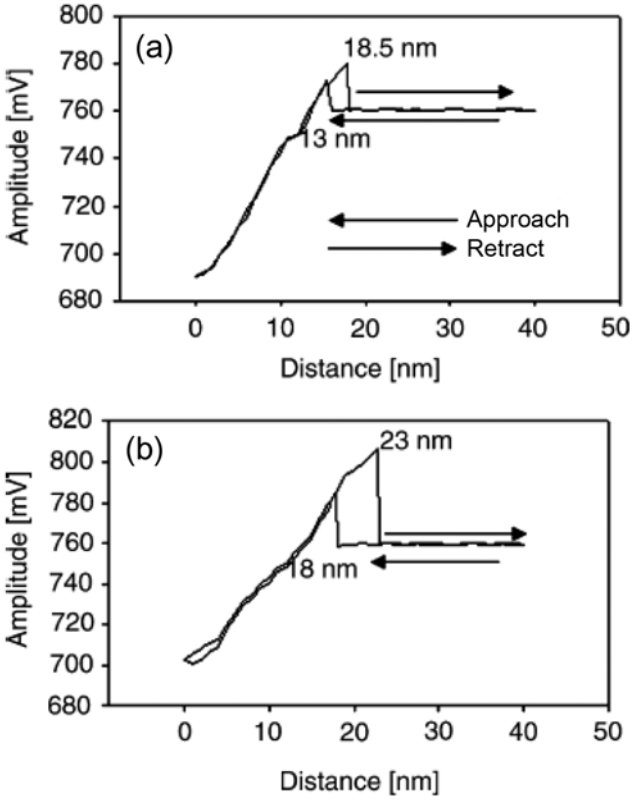

Fig. 19. Distance-vibration amplitude relations for the gaps (a) and the DNA oligonucleotides (b) in Fig. 18(d). Tip-sample interaction starts at the distance 13 nm for the approach and ends at 18.5 nm for the retraction (a). The vibration amplitude of immobilized DNA oligonucleotides is slightly larger than that of the gaps in the distance 0 position.

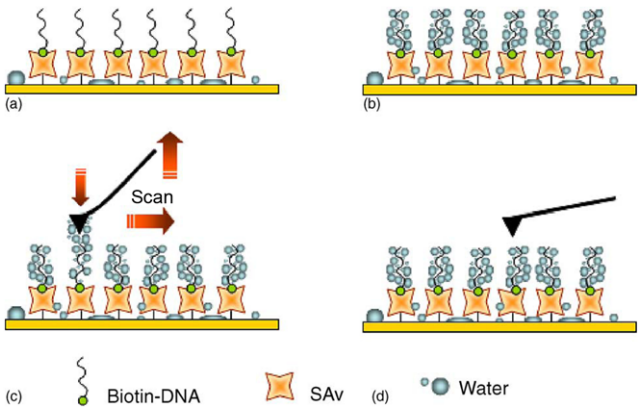

Fig. 20. A schematic illustration for the surface property changes and the imaging mechanism. In a normal condition (a), water is located in the lower parts, as explained by the gravimetric force and the hydrophobic property of the SAv molecules. By incubating the sample in a high humidity chamber (b), the vapor in the air accumulates around the hydrophilic DNA oligonucleotides with accumulation between the gaps. During imaging (c), the water around DNA oligonucleotides produces a strong capillary force and delays tip separation. After scanning (d), the water reassembles to the original hydrophilic oligonucleotides.

Amplitude-distance relations for the strong signals were measured to investigate the tip-sample interaction. As shown in Fig. 19, humidity-controlled surfaces have larger vibration amplitude values than that of the normal solid surface. The normal amplitude is approximately 0 mV at a solid surface [158]. Therefore, it means the tip still strongly vibrates near the surface. In this way, the position of strong phase signals can be explained by the movable surface (liquid phase).

As a summary of the phase mapping, we suggest an AFM imaging mechanism like that illustrated in Fig. 20. In the mechanism, we stress the role of DNA oligonucleotide as a hydrophilic center on the relatively hydrophobic SAv surface. When relative surface humidity increases with increasing incubating time, the hydrophilic DNA oligonucleotides gather moisture component. For that reason, wet conditions can be formed easily in the hydrophilic DNA oligonucleotides, engendering a strong phase lag in the imaging.

For the affinity force measurement, interaction forces between each peptide probe **1-4** and profilin molecules were examined using force curve measurements in a Tris buffer solution. Fig. 21(a) shows a typical force curve obtained between the profilin molecules and the probe **1**. In the retraction part, the force curve shows several peaks of the negative direction. The negative direction indicates an interaction involving attraction. In contrast, the force curve between unmodified surface and peptide probe **1** shows no peak (Fig. 21(b)). This difference suggests that the retraction forces demonstrated by Fig. 21(a) resulted from a specific affinity involving the probe **1** and the profiling molecules. In an effort to estimate the strength of this specific affinity, the maximum attraction force was determined for each force curve of the probe **1** against the profiling molecules, and this force was summarized in the form of a histogram. The histogram adapted well to a Gaussian curve, and the peak position was at 652 pN (average 633 pN). In contrast, the average maximum re-

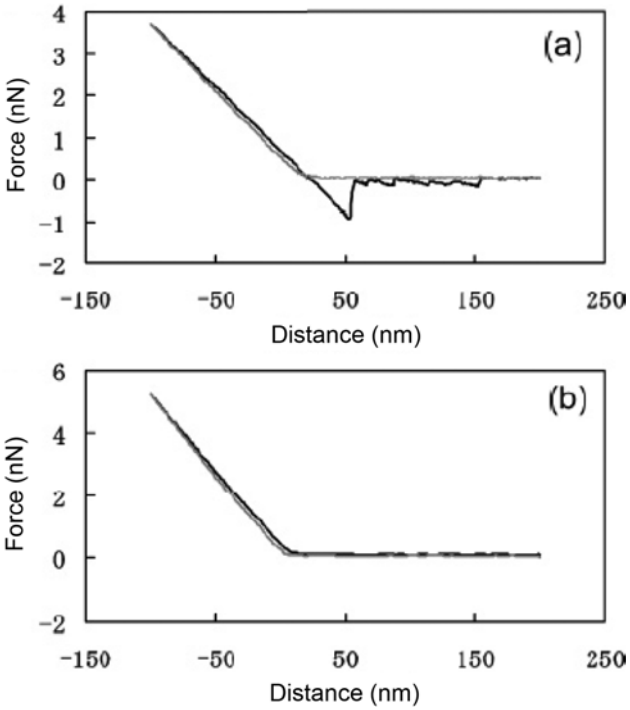

Fig. 21. Representative force curve obtained between the probe 1 and (a) profilin or (b) Tris. The gray line represents the force for the approaching step, and the black line represents the force for the retracting step.

traction force of the probe **1** against the substrate was 120 pN. The difference in the average values confirms that the probe **1** has a specific affinity for the profiling molecules. To investigate the dependency of the affinity on the peptide sequence, force curves for the peptide probes **2**, **3**, and **4** were examined in the same manner as with the peptide probe **1**. Additionally, a control experiment was performed by adding the free peptide probe **1** to the fluid cell of the profilin-immobilized substrate. In the experiment comprising the addition of the free peptide probe, although peptide probe **1** showed an averaged retraction force to blocked profilin of 158 pN, the highest peak of the histogram was at around 60 pN. Since the highest peaks for probes **2** and **3** were also near 60 pN, the nonspecific binding force of the probe **1** was at around 60 pN.

In Table 1, the averaged forces show that, of the four peptide probes examined, probe **1** has the highest affinity force for the profiling molecules. The results support a specific interaction of probe **1** with the profiling molecules. Probe **4** has the smallest retraction force (Table 1). Since probe **4** does not contain the GP5 sequence, the retraction force for probe **4** (93 pN) is supposed to present the nonspecific binding force. This sequence-dependent affinity was also demonstrated when comparing the retraction forces of probes **2** and **3**. Nevertheless, although probes **2** and **3** are composed of the same number of amino acids, the averaged retraction force of probe **2** was approximately twice as large as that of probe **3**. This large retraction force is reasonable since probe **2** includes the GP5 sequence that presents one segment of the binding sequence of VASP to the profilin molecules (with three consecutive GP5 sequences). While the previous study reported a low affinity interaction between a single repeat peptide (GP5) and the profiling molecules, the averaged retraction force of GP5 (probe **2**) in this study is large. This relatively large force would result if probe 2 was immobilized at a high density and where more than a probe molecule bound to the profiling molecules concurrently. The averaged retraction force of peptide probe **1** (633 pN) would include multiple interactions rather than just a single molecule interaction. Under these experimental conditions, multiple interactions consistently occur, since the estimated contact area between the mica surface and the tip corresponds to tens of the profilin molecules, as the occupation area for a single profilin molecule is 9 nm [160,170]. To verify the retraction force of a single molecular interaction, the obtained force curve was analyzed further. For example, the force curve shown in Fig. 21(a) shows a maximum retraction force at 625 pN, followed by several small retraction forces around 80 pN.

Table 1. Averaged retraction force observed between each peptide probe and profilin (or blocked profilin)

Cantilever	Substrate	Retraction force (pN)
Peptide probe **1**	Profilin	633
Peptide probe **2**	Profilin	422
Peptide probe **3**	Profilin	219
Peptide probe **4**	Profilin	93
Peptide probe **1**	Profilin blocked with peptide probe **1**	158

NANO-DIAGNOSIS AND NANO-SENSING SYSTEM USING SNOAM

In 1928, E. H. Synge theorized that optical image resolution is not limited by the wavelength of the light but is limited by the size of microscopic holes; thus, the limitation of far-field diffraction can be overcome by forming a microscopic hole smaller than the wavelength of the light. Based on the theory, a scanning near-field optical microscopy (SNOM) was invented to overcome the magnification and resolution restricted by the light diffraction phenomenon by

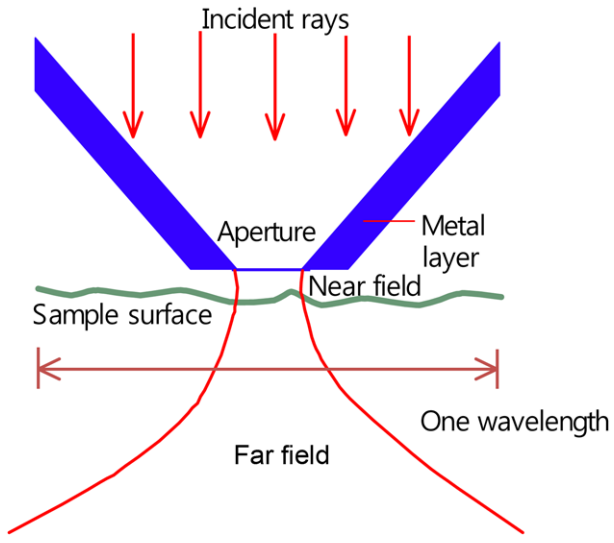

Fig. 22. The principle of near-field optical microscopy.

emitting or receiving photons via sharp optical fibers with holes sized in tens of nanometers, and optical images beyond the optical diffraction limit could be obtained [171]. Several types of SNOM were proposed depending on the methods to maintain the distance between the probe and the sample, and the principles of the measurement. In this review, mainly focusing on scanning near-field optical atomic force microscopy (SNOAM) developed by Seiko Instruments Inc., the principles and applications of nano-diagnosis will be briefly introduced. The basic measuring principle of SNOM and/or SNOAM is presented in Fig. 22.

The cantilever in the SNOAM was designed to be operated in all AFM modes by bending the optical fiber probe. As described in Fig. 22, forming a small aperture smaller than the wavelength of the light at the end of the probe and bringing it close to the sample surface in the distance shorter than the wavelength, the light obtained by the scattering on the surface reflects strongly the refractive index of the sample surface. An optical image with high resolution superior to the wavelength is obtained by scanning the probe in a two-dimensional way. Compared to the conventional optical microscopes that have resolution of approximately half of the light wavelength, SNOAM is estimated to obtain resolution of approximately 1/20th of the light wavelength. Thus, SNOAM is thought to be the most appropriate to assess the optical characteristics of small areas or to obtain high resolution optical images [172].

Based on the distance control system of Z axis that maintains the distance between the probe and the sample, the SNOM modes are mainly classified into STM [173], transient light intensity [174], shear force [175], and AFM [176-179]. The AFM mode SNOM uses an AFM cantilever as an optical probe. Until now, the method that uses fluorescence from fluorescent materials which were filled at the end of the probe as micro light source after bending the glass capillary tube to form the cantilever and the method combining PSTM and AFM that transiently scatter the light on the silicon nitride cantilever probe have been reported [176,177].

The AFM mode scanning near-field optical atomic force microscope (SNOAM or SNOM/AFM) developed by the authors' group enables the optical fiber probe to be used as the AFM probe by bending the optical fiber probe [178]. Besides a transmission measuring mode, samples can be also observed with PSTM mode and reflection measuring mode by using the optical fiber probe with an aperture. This AFM control technique is a stable controlling method due to the sufficient accumulation of the related techniques. In particular, one of the advantages of AFM mode SNOM is that it can be applied to the measurement in liquid [179]. Compared to the flat-type micro cantilever, the optic-fiber probe has an advantage of getting decreased viscosity resistance from the fluid during the vibration in liquid due to its cylindrical shape.

SNOAM will be able to be applied to not only the observation of optical properties in small areas, such as optical devices, semiconductor materials, and organic thin-film, but also biological science fields. In addition, its application to processing technology or memory technology is also considered. In the current review, the principles and applications of nano-diagnosis using SNOAM in the authors' group will be briefly introduced.

1. Principle of the Nano-diagnosis Based on the SNOAM

Many types of scanning near-field optical microscopy (SNOM) have been developed with respect to the tip-sample distance control method [172] such as scanning tunneling microscopy [171], lateral shear force [175], contact mode atomic force microscopy [176,177], and the dynamic mode AFM [178,180]. In SNOAM, an optical fiber with a sharpened tip was bent so that probe could be used as a cantilever for AFM, and the vibration amplitude of the cantilever was held constant during scanning. SNOAM has an advantage over other SNOM systems in that it allows observation in liquids [179]. It is safely applicable for observation of soft samples with varying greatly in height. SNOAM may be also superior in liquid to other cyclic contact AFMs which use flat type cantilevers [181-184] because the optical-fiber cantilever of SNOAM is round, which helps to reduce the viscous resistance of the liquid. SNOAM is an excellent tool to observe biological materials because it simultaneously provides topographic and optical images with high resolution. The resolution of topographic and optical images is much higher than that of conventional far-field microscopy. It also has the advantage for providing various kinds of information such as fluorescence images and spectrographs in a submicron area [178].

2. Visualizing a Hybridized PNA Probe on a DNA Molecule

The direct determination of specific gene location using fluorescence in situ hybridization (FISH) technique has become an important method for investigating DNA and chromosomes [185,186]. Usually, conventional far-field fluorescence microscopy is used for the FISH technique to detect the location of a specific gene on a DNA molecule. Given that the far-field optical resolution at room-temperature cannot exceed 300 nm [187-189], the resolution of the DNA mapping has been limited to 1 kbp. Furthermore, with a resolution of 300 nm, the background signals from free fluorescence molecules can be misinterpreted as signals from hybridized sites. In particular, discriminating the real signal from the background is a serious problem requiring a clear solution when the sequence indicating probe is labeled with a single dye molecule. In an effort to determine short sequence location or sequence specific function, a high-resolution imaging tool such as scanning probe microscopy (SPM) is required.

A PNA probe is smaller than that of dsDNA; furthermore, when the DNA strands are long, the precise target location cannot be easily determined because it requires not only complete DNA stretching but also both the wide area imaging and the highly magnified imaging [190] with other high resolution SPM methods. The differentiation of closely located targets is equally difficult to determine from only the height information derived from obtained topographic images. For a solution to the current problems, a pluralistic approach is ideal, and SNOAM was used to obtain high-resolution fluorescence and surface images simultaneously. SNOAM can characterize a sample better than other SPMs that determine the sample surface only by a force interaction.

In SNOAM, a bent optical fiber probe functions as a microcantilever of AFM [139,191-193]. Thus, SNOAM has clear advantages including ease of operation and assembly compared to other shear force mode instruments because the arrangement of the optical probe does not obstruct the illuminating sample and allows for the utilization of conventional AFM equipment. We have visualized hybridized-peptide nucleic acid (PNA) on a stretched DNA strand SNOAM in an effort toward investigating the possibility of discriminating continuous DNA sequences on the scale of a few tens of nanometers.

The PNA probe, composed of a 15-mer series sequence, was self-designed for hybridizing to the top part of the ea47 gene within the λ-DNA molecule (48, 502 bp, 16.5 μm). Alexa 532 pigment (A532, Molecular Probes, excitation maximum 532 nm/emission maximum 554 nm) was conjugated to the 5′ end of the PNA probe. The PNA probe was hybridized to λ-DNA molecules in aqueous solution at a temperature of 80 °C.

Before the SNOAM observation, the samples were stained using the DNA intercalating dye, YOYO-1 (Molecular Probes, excitation maximum 491 nm/emission maximum 509 nm), at a mixing ratio of 1 : 5 (dye : bp). In an effort to determine the precise location of the hybridized PNA probe, we stretched the DNA strands on a specially laminated mica/cover slip substrate [193] using a spin stretching method [194].

The SNOAM instrument utilized a conventional AFM controller (SPI 3800, Seiko Instruments), which has a dynamic force mode (DFM) function [193]. In the measurement, the fluorescence from A532 and YOYO-1 can be imaged independently using different light sources.

Fig. 23 shows 50 nm resolution near-field fluorescence images for YOYO-1 (a), A532 (b), and an overlapped image (c). The overlapped image was produced to visualize the PNA hybridization position in the DNA molecules similar to the well-known far-field technique. The optical resolution was estimated by a mean resolution of 10 continuous scans for the A532 light spot at a full width half maximum (FWHM). In Fig. 23(a), the DNA molecules are visible as continuous lines by the intercalated YOYO-1 fluorescence data except near the center of the DNA molecules. These non-fluorescence regions were reproducible in the experiments although the length of the regions was largely influenced by the dye/bp mixing ratio and the stretching conditions. In the case of the far-field image, the region was not clearly obtainable because of the far-field optical resolution limit. In addition, as reported previously, the nonhybridized λ-DNA molecule did not show such non-fluorescence regions in the SNOM images [198]. Therefore, the non-fluorescence area as observed in Fig. 23(a) can be a kind of evidence for the hybridized position of PNA and the region nearby the position. This result suggests that PNA invasion into dsDNA makes a change in dsDNA structure in a long distance. Relative results have been reported for the intercalation difference of YOYO-1 to ssDNA and dsDNA [193]. It has been explained that the hybridization of PNA probes weakens the hydrogen bond around the hybridized position in DNA strands [195-198]. Furthermore, we have reported the heterogeneous intercalation of YOYO-1 to DNA strands [195-198]. The main factor responsible for the gap in YOYO-1 by the PNA probe remains to be clarified. Nevertheless, the results of heterogeneous intercalation suggest that YOYO-1 intercalation is very sensitive to the conditions of DNA strands. In Fig. 23(c), the length of the non-fluorescence region is about 200 nm. In our experiments, the gap length was observed in a range of 100-1,000 nm under the experimental conditions employed. This length is much longer than the length of the PNA probe. Although the mechanism responsible for this non-

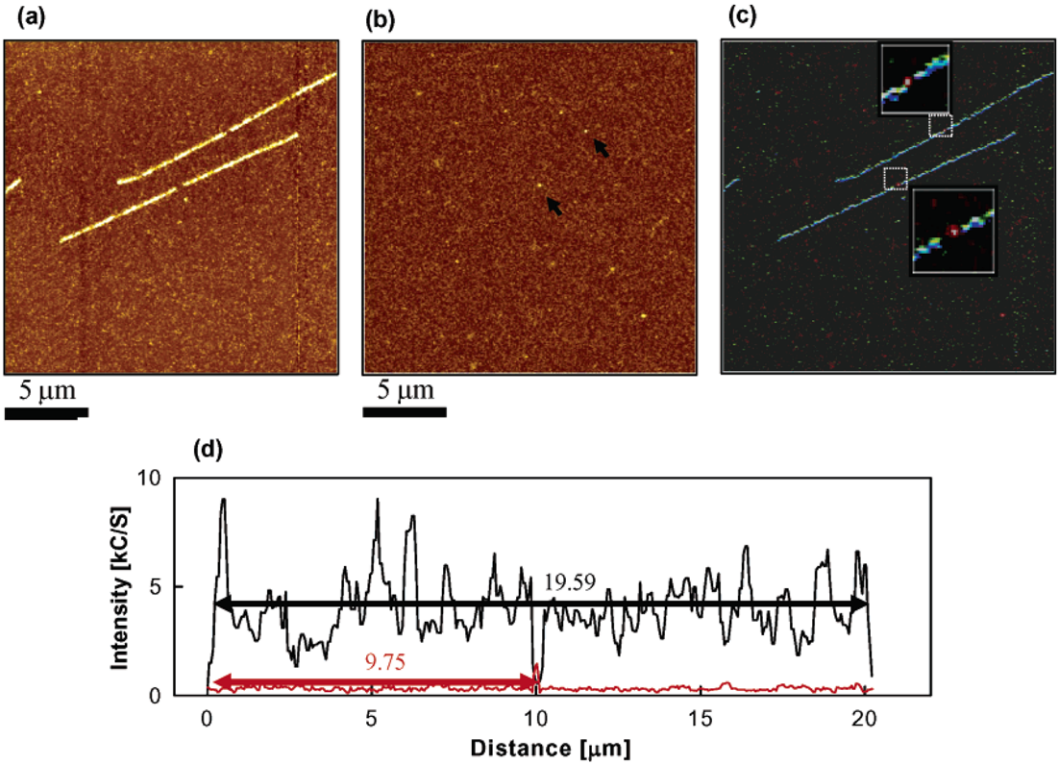

Fig. 23. Near-field fluorescence images for the single target DNA FISH samples by fluorescence resolution of 50 nm. (a) the fluorescence image of YOYO-1, (b) the fluorescence images of A532, and (c) the overlapped images of (a) and (b). In panel (c), the YOYO-1 and A532 fluorescence signals are artificially colored in blue and red, respectively. (d) line profile analysis results for the YOYO-1 and A532 fluorescence over the DNA lengths. All the image areas are 25×25 mm^2 with 512×256 data formats. The small insets in panel (c) show the PNA probe hybridized areas.

fluorescence region around the PNA probe possibly relates to the same mechanism responsible for the non-fluorescence region existing in normal DNA strands, more careful inspection is required to understand the real mechanism in the future. The location of the hybridized PNA has been determined by line profile analyses to the DNA length direction. In Fig. 23(d), the hybridized position is located in the middle of the DNA strands, and the distance from one end of the DNA to the center of the A532 spot is 9.75 μm. As the measured length of DNA strand was 19.59 μm in Fig. 23(a), the exact stretching factor can be calculated to 19.59 μm/48.5 kbp= 0.404 μm/kbp. Therefore, the PNA hybridization position is calculated to 9.75 μm/0.404 μm/kbp=24.1 kbp. Although the calculated value approximately matched the real position of the sequence (23,904 bp), the calculated value contains an error generated by the heterogeneity in the DNA stretching and the accuracy of the fluorescence measurement.

As reported by Bennink et al. [190], the length of the DNA molecules can vary depending on the applied stretching force or the YOYO-1 intercalation conditions. In the case of spin-stretching with a Mg^{2+} soaked mica surface, a standard length of 16.9±4.3 μm for λ-DNA molecules was reported [194] at a spin speed of 5,500 rpm and could be accounted for in terms of the difference in applied stretching force to each DNA molecule. In addition, surface conditions such as charge distribution or surface roughness can influence the stretching since these properties influence the static interaction between the DNA molecules and the mica surface. The heterogeneity of the YOYO-1 intercalation as documented in previous reports [191,193] also suggests the possibility of an effect derived from sequence heterogeneity to the stretching since the YOYO-1 intercalation can affect the length of DNA obtained. The location error also increases with spin speeds lower than 5,500 rpm since the meandering of DNA occurs in the stretching process under the experimental conditions employed. As various reports [199] have documented the sequence-specific interaction of PNA probes to target DNA sequences, the major error factor in determining the precise location is associated with the stretching homogeneity.

When the sample and sample surface were sufficiently purified and deionized, a high resolution topographic image was simultaneously obtainable as shown in Fig. 24. In Fig. 24(a) and 24(b), the topographic image of a DNA strand was successfully obtained with a whole DNA length of 19.4 μm. Because of the wide imaging range of 20×20 μm^2, the fluorescence spot from the hybridized PNA probe could not be confirmed in Fig. 24(b). By enlarging the middle of the DNA strand to 2×2 μm^2 as shown in Fig. 24(c) for topography and Fig. 24(d) for the fluorescence image, a few small fluorescence spots were observed in Fig. 24(d). Fig. 24(e) shows an overlapped image of Fig. 24(c) on 24(d) and shows that a fluorescence spot is on the DNA strand.

Line profiles of the DNA topography for the hybridized site and other sites located close to the spot site of Fig. 24(e) are shown in Fig. 24(f). In Fig. 24(f), the topographic line profiles show differences from each other. As the tip radius of the peak is larger than the radius of the DNA strand, the DNA width in the image is larger than its real radius [193]. Therefore, the wide width in the topographic line profiles can be used to confirm the possibility of PNA probe hybridization [200,201], but it does not make any sense without the fluorescence signals, given the various possible measurement errors. As shown in the topography and fluorescence overlapped image (Fig. 24(e)), the topography and the fluorescence image are in agreement with the hybridized site. Additionally, a similar topographic change was confirmed using a highly magnified tapping mode AFM image with a normal Si AFM cantilever. Therefore,

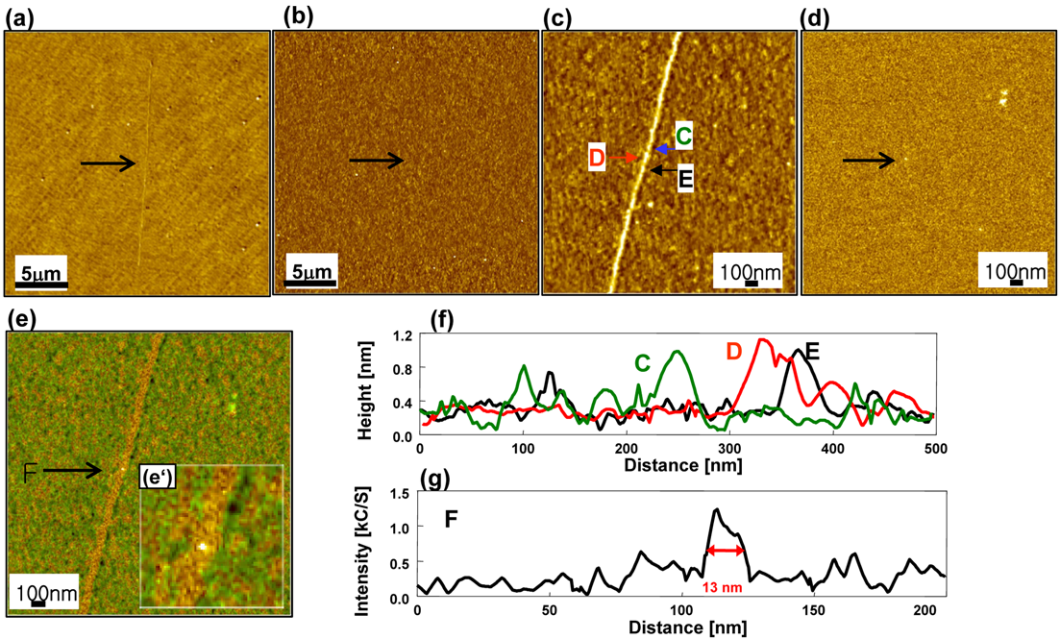

Fig. 24. Simultaneous topographic (a) and A532 fluorescence (b) images in 25×25 mm^2 area, and the respective enlarged images for the hybridized area of 2×2 mm^2 (c), (d); (e) Overlapped image of panel (c) and (d); (f) Line profiles of the topographic image of panel (c); Line profile of the fluorescence image (g). All images represent 512×256 data formats. The labels C, D, E, F correspond to each line profile analysis.

this confirms the position as the hybridization site. The line profile (Fig. 24(g)) shows that the A532 fluorescent signal is visualized as a light spot with the width of 13 nm at an FWHM, which corresponds to the best optical resolution ever reported at room temperature [187]. This resolution was reconfirmed by imaging a single fluorescence molecular immobilized sample. Although this excellent optical resolution was not highly reproducible, we have already shown that obtaining sub-20 nm single molecular fluorescence resolution was possible using the current optical probe design [139,191,192]. Single molecular fluorescence resolution of 13 nm corresponds to more than a 20-fold higher resolution than that previously reported [202] by using the deconvolution technique of conventional FISH images. As a 13 nm DNA length corresponds to 50 bp, it will be possible to distinguish adjacent regions of 50 bp using PNA probes of varying sequence with different fluorescence molecules. For this purpose, we have been developing an SNOAM combined with a spectrometer and a highly sensitive CCD camera that enables simultaneous multicolor fluorescence imaging [203]. The system can visualize multiple fluorescence images simultaneously for multiple fluorescence probes.

The technique drastically overcomes the resolution limit of the conventional FISH techniques achieved by the far-field optical microscopy and enables a direct gene mapping at a resolution in the tens of nanometers range.

CONCLUSION

We have briefly reviewed the basic principles and research trend of biosensors, nano-sensing system using QCM, and nano-diagnosis system using AFM and SNOAM. The application range of the quartz crystal has been gradually expanded, new measuring techniques that use the quartz crystal as a transducer for chemical sensors and biosensors have been also developed. In addition, as the research on the application of the quartz crystal in solution is in progress, the research results are expected to be continuously announced. SPM will be able to be applied to not only the observation of topographic properties in small areas, such as optical devices, semiconductor materials, and organic thin-film, but also functional biological science. In addition, as its application to processing technology or memory technology is also considered, future development of potential fields is also expected. In particular, low-invasive and high efficient gene delivery technology using AFM and the nano-probe that has been recently studied is expected to be applied to important cell manipulations or the induction of cell differentiation.

ACKNOWLEDGEMENTS

This research was supported partly by the Basic Science Research Program through the National Research Foundation of Korea (NRF) funded by the Ministry of Education, Science and Technology (KOSEF, 2009-0064245).

REFERENCES

1. L. C. Clark and C. Lyons, *Ann. N.Y. Acad. Sci.*, **102**, 29 (1962).
2. S. J. Updike and G. P. Hicks, *Nature*, **214**, 986 (1967).
3. I. Karube and S. Suzuki, *Ion-Selective Electrode Reviews*, **6**, 15 (1984).
4. I. Karube, *Ion-Selective Electrode Reviews*, **10**(1), 37 (1988).
5. M. Gotoh, E. Tamiya, M. Momoi, Y. Kagawa and I. Karube, *Anal. Lett.*, **20**, 857 (1987).
6. H. Muramatsu, J. M. Dicks and I. Karube, *Anal. Chim. Acta*, **197**, 347 (1987).
7. H. Hayashi, S. Sasaki, K. Ikebukuro and I. Karube, *Anal. Chim. Acta*, **197**, 127 (1996).
8. H. Muramatsu and J. M. Dicks, *Anal. Chem.*, **59**, 2760 (1987).
9. T. Lim, M. Oyama, K. Ikebukuro and I. Karube, *Anal. Chem.*, **72**(13), 2856 (2000).
10. G. H. Wu, R. H. Datar, K. M. Hansen, T. Thundat, R. J. Cote and A. Majumdar, *Nature Biotechnology*, **19**(9), 856 (2001).
11. Y. Arntz, J. D. Seeling, H. P. Lang, P. Zhang, J. P. Ramseyer, E. Mayer, M. Hegner and M. Gerver, *Nanotechnology*, **19**, 856 (2003).
12. H. Nakamura and I. Karube, *Anal. Bioanal. Chem.*, **377**(3), 446 (2003).
13. A. P. F. Turner, I. Karube and G. S. Wilson, *Biosenssors - Fundamentals and applications*, Oxford University Press, New York (1987).
14. I. Karube, *Array technologies - Handbook of biosensors and biochips*, John Wiley & Sons, New York, 857 (2007).
15. T. Takeuchi, M. Yoshida, Y. Kabasawa, E. Tamiya and I. Karube, *Anal. Lett.*, **26**, 1535 (1993).
16. M. I. Song, K. Iwata, M. Yamada, K. Yokoyama, T. Takeuchi, E. Tamiya and I. Karube, *Anal. Chem.*, **66**, 778 (1994).
17. K. Yokoyama, K. Ikebukuro, E. Tamiya, I. Karube, N. Ichiki and Y. Arikawa, *Anal. Chim. Acta*, **304**, 139 (1995).
18. K. Yagiuda, A. Hemmi, S. Ito, Y. Asano, Y. Fushinuki, C. Y. Chen and I. Karube, *Biosens. Bioelectron.*, **11**, 703 (1996).
19. I. Karube and K. Nakanishi, *Current Opinion in Biotechnol.*, **5**, 54 (1994).
20. H. Nakamura, Y. Hirata, Y. Mogi, S. Kobayashi, K. Suzuki, T. Hirayama and I. Karube, *Anal. Bioanal. Chem.*, **389**, 835 (2007).
21. I. Karube, T. Matsunaga, S. Tsuru and S. Suzuki, *Biochim. Biophys. Acta*, **444**, 338 (1976).
22. T. Takeuchi, K. Yokoyama, K. Kobayashi, M. Suzuki, E. Tamiya, I. Karube, K. Utsunomiya, O. Imai and Y. Masuda, *Anal. Chim. Acta*, **276**, 65 (1993).
23. C. Tuerk and L. Gold, *Science*, **249**, 505 (1990).
24. S. M. Nimjee, *Annu. Rev. Med.*, **56**, 555 (2005).
25. M. Schena and D. Shanlon, *Science*, **270**, 467 (1995).
26. M. Chee, R. Yang and E. Hubbell, *Science*, **274**, 610 (1996).
27. E. Marshall, *Science*, **291**, 396 (2001).
28. S. C. Terry, H. Jeman and J. B. Angell, *IEEE Trans. Electron Devices*, **26**, 1880 (1979).
29. A. Manz, N. Graber and H. M. Widmer, *Sens. Actuators. B.*, **1**, 244 (1990).
30. A. S. Blaws and W. M. Reichert, *Biomaterials*, **19**, 595 (1998).
31. G. Macbeath and S. L. Schreiber, *Science*, **289**, 1760 (2000).
32. H. Zhu and M. Bilgin, *Science*, **293**, 2101 (2001).
33. T. Kukar and S. Eckenrode, *Anal. Biochem.*, **306**, 50 (2002).
34. K. Kojima, A. Hiratsuka, H. Suzuki, K. Yano, K. Ikebukuro and I. Karube, *Anal. Chem.*, **75**, 1116 (2003).
35. K. K. Jain, *Clinica Chimica Acta*, **358**, 37 (2005).
36. Y. Matsubara and Y. Murakami, *Biosens. Bioelectron.*, **19**, 741 (2004).
37. Y. Cui and Q. Wei, *Science*, **293**, 1298 (2001).

38. J. P. Kim, B. Y. Lee, S. Hong and S. J. Sim, *Anal. Biochem.*, **381**, 193 (2008).
39. H. M. So, K. Won, Y. H. Kim, B.-K. Kim, B. H. Ryu, P. S. Na, H. Kim and J.-O. Lee, *J. Am. Chem.Soc*, **127**, 11906 (2005).
40. J. Hahm and C. M. Lieber, *Nano Lett.*, **4**(1), 51 (2004).
41. K. Besteman, J. O. Lee, F. G. M. Wiertz, H. A. Heering and C. Dekker, *Nano Lett.*, **3**(6), 727 (2003).
42. F. Kurusu, H. Tsunoda, A. Saito, A. Tomita, A. Kadota, N. Kayahara, I. Karube and M. Gotoh, *Analyst*, **131**(12), 1292 (2006).
43. R. J. Chen, H. C. Choi, S. Bangsaruntip, E. Yenilmez, X. W. Tang, Q. Wang, Y. L. Chang and H. J. Dai, *J. Am. Chem. Soc.*, **126**(5), 1563 (2004).
44. C. Jianrong and M. Yuqing, *Biotechnology Advances*, **22**, 505 (2004).
45. T. Vo-Dinh, *Appl. Spectr.*, **41**, 735 (1987).
46. M. Brian, *Anal. Biochem.*, **277**, 25 (2000).
47. P. M. Kasili and T. Vo-Dinh, *J. Nanosci. Nanotechnol.*, **5**(12), 2057 (2005).
48. M. B.Wabuyele and T. Vo-Dinh, *Anal. Chem.*, **77**(23), 7810 (2005).
49. T. Vo-Dinh and P. Kasili, *Anal. Bioanal. Chem.*, **382**(4), 918 (2005).
50. Y. C. Cao and R. Jin, *Science*, **297**, 1536 (2002).
51. J. M. Nam, S. Stoeva and C. A. Mirkin, *J. Am. Chem. Soc.*, **126**, 5932 (2004).
52. S. I. Stoeva, J. S. Lee, T. Shad and C. A. Mirkin, *Angew. Chem. Int. Ed.*, **45**, 3303 (2006).
53. J. Liu and Y. Lu, *J. Am. Chem. Soc.*, **125**, 6642 (2003).
54. J. Liu and Y. Lu, *Nanotechnology*, **14**, 353 (2004).
55. A. Star, E. Tu and J. Niemann, *PNAS*, **103**, 921 (2006).
56. D. W. Park, Y. H. Kim, B. S. Kim, H. M. So, K. Won, J. O. Lee, K. Kong and H. Chang, *J. Nanosci. Nanotechnol.*, **6**, 3499 (2006).
57. R. Brown and E. T. Zellers, *Enviromental monitoring*, VCH Publishers Inc., New York, 529 (1989).
58. G. Z. Sauerbrey, *Zeitscrift fuer Physic*, **155**, 206 (1959).
59. W. H. King, *Anal. Chem.*, **36**, 1735 (1964).
60. J. Hlavay and G. Guilbault, *Anal. Chem.*, **49**, 1890 (1977).
61. K. K. Kanazawa and J. G. Gordon, *Anal. Chim. Acta*, **175**, 99 (1985).
62. H. Muramatsu, E. Tamiya and I. Karube, *J. Membrane Sci.*, **41**, 281 (1989).
63. H. Muramatsu, E. Tamiya and M. Suzuki, *Anal. Chim. Acta*, **215**, 91 (1988).
64. H. Muramatsu, E. Tamiya, M. Suzuki and I. Karube, *Anal. Chim. Acta*, **217**, 321 (1989).
65. H. Muramatsu, X. Ye, M. Suda, T. Sakuhara and T. Ataka, *Electroanal. Chem.*, **322**, 311 (1992).
66. H. Yufan, W. Ying, Z. Guoyi and W. Erkang, *Electroanal. Chem.*, **440**, 65 (1997).
67. D. Orata and D. A. Buttry, *J. Am. Chem. Soc.*, **109**, 3574 (1987).
68. J. M. Kim, S. M. Chang and H. Muramatsu, *J. Electrochem. Soc.*, **146**, 4544 (1999).
69. J. M. Kim, S. M. Chang and H. Muramatsu, *Polymer*, **40**, 3291 (1999).
70. S. M. Chang, J. M. Kim, H. Muramatsu, T. Ataka, W. J. Cho and C. S. Ha, *Polymer*, **37**, 3757 (1996).
71. J. M. Kim, S. M. Chang and H. Muramatsu, *Appl. Phys. Lett.*, **74**, 466 (1999).
72. J. M. Kim, J. Y. Park, S. H. Song, H. Muramatsu, B. J. Lee and S. M. Chang, *Sens. Act. B*, **76**, 74 (2001).
73. J. M. Kim, S. H. Kim, T. Ohashi, H. Muramatsu, S. M. Chang and W. S. Kim, *Bioprocess Biosyst. Eng.*, **33**, 39 (2010).
74. P. L. Konash and G. Bastiaans, *Anal. Chem.*, **52**, 1929 (1980).
75. C. S. Lu and O. Lewis, *Appl. Phys.*, **43**, 4385 (1972).
76. H. K. Pulker, E. Benes, D. Hammer and E. Sollner, *Thin Solid Films*, **32**, 27 (1976).
77. A. P. Glassford and M. J. Vac, *Sci. Technol.*, **75**, 1836 (1978).
78. V. Mecea and V. Burcur, *Thin Solid Films*, **60**, 73 (1979).
79. R. A. Crane and G. Fisher, *Appl. Phys. D*, **12**, 2019 (1979).
80. H. Muramatsu, E. Tamiya and I. Karube, *Anal. Chem.*, **60**, 2142 (1988).
81. H. Muramatsu and K. Kimura, *Anal.Chem.*, **64**, 2502 (1992).
82. H. Muramatsu, A. Egawa and K. Ataka, *Electroanal. Chem.*, **388**, 89 (1995).
83. D. A. Buttry and M. D. Ward, *Chem. Rev.*, **92**, 1355 (1992).
84. J. E. Roederer and G. J. Bastiaans, *Anal. Chem.*, **55**, 2333 (1983).
85. M. Thompson, C. L. Arthur and G. K. Dhaliwal, *Anal. Chem.*, **58**, (1988).
86. H. Muramatsu, K. Kajiwara, E. Tamiya and I. Karube, *Anal. Chim. Acta*, **188**, 257 (1986).
87. H. Muramatsu, Y. Watanabe, M. Hikuma, T. Ataka, I. Kubo, E. Tamiya and I. Karube, *Anal. Lett.*, **22**, 2155 (1989).
88. T. Okada, Y. Yamamoto, H. Miyachi, I. Karube and H. Muramatsu, *Biosens. Bioelectron.*, **22**, 1480 (2007).
89. H. Matsuoka, I. Karube, N. T. K. Nhung and S. Suzuki, *Denki Kagaku*, **50**, 946 (1982).
90. H. Matsuoka, E. Tamiya and I. Karube, *Anal. Chem.*, **57**, 1998 (1985).
91. K. Nisson and K. Mosbach, *Biochem. Biophys. Res. Commun.*, **102**, 449 (1981).
92. H. Muramatsu, K. Kimura, T. Ataka, R. Honma, Y. Miura and I. Karube, *Biosens. Bioelectron.*, **6**, 35 (1991).
93. R. Homma, Y. Takeda, I. Karube, K. Kimura and H. Muramatsu, *Anal. Biochem.*, **204**, 398 (1992).
94. F. B. Bang, *Johns Hopkins Hosp*, **98**, 325 (1956).
95. J. Levin and F. B. Bang, *Johns Hopkins Hosp*, **115**, 265 (1964).
96. S. Nakamura, T. Morita, T. Harada-Suzuki, S. Iwanaga, K. Takahashi and M. Niwa, *Biochem*., **92**, 781 (1982).
97. H. Oishi, T. Takaoka, Y. Hatayama, T. Matsuo and Y. Sakata, *Parenter. Sci. Technol.*, **39**, 194 (1985).
98. R. Homma, *Pharm. Technol. Jpn*., **1**, 11 (1985).
99. C. S. Chen, M. Mrksich, S. Huang, G. M. Whitesides and D. E. Ingber, *Science*, **276**, 1425 (1997).
100. D. A. Flusberg, Y. Numaguchi and D. E. Ingber, *Mol. Biol.*, **12**, 3087 (2001).
101. D. Stamenović and M. F. Coughlin, *Theor. Biol.*, **201**, 63 (1999).
102. J. C. Dubois, C. Souchier, M. L. Couble, P. Exbrayat and M. Lissac, *Biomaterials*, **20**, 1841 (1999).
103. F. M. M. Morel, R. F. Baker and H. Wayland, *Cell. Biol.*, **48**, 91 (1971).
104. D. J. O'Donovan, J. P. Katkin, T. Tamura, R. Husser, X. Xu, C. V. Smith and S. E. Welty, *Am. J. Respir. Cell. Mol. Biol.*, **20**, 256 (1999).
105. K. Nomura, H. Imai, T. Koumura, M. Arai and Y. Nakagawa, *Biol. Chem.*, **274**, 29294 (1999).
106. H. W. Kang, K. Ida, Y. Yamamoto and H. Muramatsu, *Anal. Chim. Acta*, **624**, 154 (2008).
107. H. W. Kang and H. Muramatsu, *Biosens. Bioelectron.*, **24**, 1318 (2009).

108. G. Binning, H. Rohrer, C. Gerber and E. Weibel, *Phys. Rev. Lett.*, **49**, 57 (1982).
109. G. Binning, C. F. Quate and C. Gerber, *Phys. Rev. Lett.*, **56**, 930 (1986).
110. H. Ohtani, R. J. Wilson, S. Chiang and C. M. Mactec, *Phys. Rev. Lett.*, **60**, 2398 (1988).
111. D. P. E. Smith, A. Bryant, C. F. Quate, J. P. Rabe, C. Gerber and J. D. Swalen, *Proc. Natl. Acad. Sci. USA*, **84**, 969 (1987).
112. J. S. Foster and J. E. Frommer, *Nature*, **333**, 542 (1988).
113. W. M. Heckl, D. P. E. Smith, H. K. G. Binnig, T. W. Hansch and J. Maddocks, *Proc. Natl. Acad. Sci. USA*, **88**, 8003 (1991).
114. M. J. Allen, M. Balooch, S. Subbiah, R. J. Tench, W. Siekhous and R. Balhorn, *Scanning Microsc.*, **5**, 625 (1991).
115. S. A. C. Gould, O. Marti, B. Drake, L. Hellemans, C. E. Bracker, P. K. Hansma, N. L. Keder, M. M. Eddy and G. D. Stucky, *Nature*, **332**, 332 (1988).
116. J. Mou, W. Sun, J. Yan, W. S. Yang, C. Liu, Z. Zhai, Q. Xu and Y. Xie, *Vac. Sci. Technol.*, **B9**, 15569 (1991).
117. J. P. Ruppersberg, J. K. H. Härber, G. Gerber and G. Binnig, *FEBS Letters*, **257**, 460 (1989).
118. R. Guckenberger, B. Hacker, T. Hartmann, T. Schubani, Z. Wang, W. Wiegrabe and W. Baumeisyer, *Vac. Sci. Technol.*, **B9**, 1227 (1991).
119. J. A. N. Zasadzinski, J. Schneir, J. Gurley, V. B. Elings and P. K. Hansma, *Science*, **239**, 1013 (1988).
120. S. Singh and D. J. Keller, *J. Biophys.*, **60**, 1401 (1991).
121. J. N. Lin, B. Drake, A. S. Lea, P. K. Hansma and J. D. Andrade, *Langmuir*, **6**, 509 (1990).
122. C. H. Olk, J. Heremans, P. S. Lee, D. Dziedzic and N. E. Sargent, *Vac. Sci. Technol.*, **B9**, 1628 (1991).
123. S. Han, C. Nakamura, Y. Imai, N. Nakamura and J. Miyake, *Biosens. Bioelectron.*, **24**, 1219 (2008).
124. S. Han, C. Nakamura, I. Obataya and N. Nakamura, *Biochem. Biophys. Res. Co.*, **332**, 633 (2005).
125. S. Han, C. Nakamura, I. Obataya, N. Nakamura and J. Miyake, *Biosens. Bioelectron.*, **20**, 2120 (2005).
126. S. Han, C. Nakamura, I. Obataya, N. Nakamura and J. Miyake, *Biosens. Bioelectron.*, **24**, 1219 (2008).
127. S. Han, C. Nakamura, N. Kotobuki, I. Obataya, H. Ohgushi, T. Nagamune and J. Miyake, *Nanomedicine*, **4**, 215 (2008).
128. C. Nakamura, H. Kamiishi, N. Nakamura and J. Miyake, *Electrochemistry*, **76**, 586 (2008).
129. I. Obataya, C. Nakamura, S. Han, N. Nakamura and J. Miyake, *Nano Lett.*, **5**, 27 (2005).
130. I. Obataya, C. Nakamura, S. Han, N. Nakamura and J. Miyake, *Biosens. Bioelectron.*, **20**, 1652 (2005).
131. I. Obataya, C. Nakamura, S. Han, N. Nakamura and J. Miyake, *Nanobiotechnology*, **1**, 347 (2005).
132. R. Wiesendanger, *Scanning probe microscopy and spectroscopy*, Cambridge University Press, New York (1994).
133. P. Hinterdorfer and Y. F. Dufrene, *Nature Methods*, **3**(5), 347 (2006).
134. D. Leckband, *Ann. Rev. Biophys. Biomol. Struct.*, **29**, 126 (2000).
135. P. F. Luckham and K. Smith, *Faraday Discuss*, **111**, 307 (1999).
136. J. W. Park, H. Y. Lee, J. M. Kim, R. Yamasaki, T. Kanno, H. Tanaka, H. Tanaka and T. Kawai, *J. Biosci. Bioeng.*, **97**, 29 (2004).
137. J. M. Kim, H. S. Jung, J. W. Park, H. Y. Lee and T. Kawai, *Anal. Chim. Acta*, **525**, 151 (2004).
138. J. M. Kim, T. Ohtani, J. Y. Park, S. M. Chang and H. Muramatsu, *Ultramicroscopy*, **91**, 139 (2002).
139. J. M. Kim, T. Hirodse, S. Sugiyama, T. Ohtani and H. Muramatsu, *Nano Lett.*, **4-11**, 2091 (2004).
140. K. O. Greulich, *Chem. Phys. Chem.*, **6**, 2458 (2005).
141. F. J. Giessibl, *Mater. Today*, 32 (2005).
142. J. R. Withers and D. E. Aston, *Adv. Collid Interf. Sci.*, **120**, 57 (2006).
143. T. Junno, S. B. Carlsson, H. Xu, L. Montelius and L. Samuelson, *Appl. Phys. Lett.*, **72**, 548 (1998).
144. Y. Okada, S. Amano, Y. Iuchi, M. Kawabe and J. S. Harris, *Electron. Lett.*, **34**, 1262 (1998).
145. S. Sasa, T. Ikeda, C. Dohno and M. Inoue, *Japanese J. Appl. Phys., Part 1*, **36**, 4065 (1997).
146. S. Sasa, S. Yodogawa, S. Ohya and M. Inoue, *Japanese J. Appl. Phys., Part 1*, **40**(3B), 2026 (2001).
147. P. M. Campbell, E. S. Snow and P. J. McMarr, *Phys B: Condens Matter*, **227**(1–4), 315 (1996).
148. J. I. Shirakashi, K. Matsumoto, N. Miura and M. Konagai, *Japanese J. Appl. Phys., Part 2*, **36**(9), 1257 (1997).
149. R. G. Sosnowski, E. Tu, W. F. Butler, J. P. O'Connell and M. J. Heller, *Proc. Natl. Acad. Sci. U.S.A.*, **94**, 1119 (1997).
150. M. Masarik, R. Kizek, K. J. Kramer, S. Billova, M. Brazdova, J. Vacek, M. Bailey, F. Jelen and J. A. Howard, *Anal. Chem.*, **75,** 2663 (2003).
151. F. Caruso, E. Rodda, D. N. Furlong, K. Niikura and Y. Okahata, *Anal. Chem.*, **69**, 2043 (1997).
152. C. Larsson, M. Rodahl and F. Hook, *Anal. Chem.*, **75**, 2080 (2003).
153. J. Wang, *Anal. Chim. Acta*, **469**, 63 (2002).
154. J. Tamayo and R. Garcia, *Langmuir*, **12**, 4430 (1996).
155. V. J. Morris, A. R. Kirby and A. P. Gunning, *Atomic force microscopy for biologists*, Imperial College Press, London (1999).
156. S. J. T. v. Noort, K. O. v. d. Werf, B. G. d. Grooth, N. F. v. Hulst and J. Greve, *Ultramicroscopy*, **69**, 117 (1997).
157. M. Argaman, R. Golan, N. H. Thomson and H. G. Hansma, *Nucl. Acid. Res.*, **25**, 4379 (1997).
158. J. P. Cleveland, B. Anczykowski, A. E. Schmid and V. B. Elings, *Appl. Phys. Lett.*, **72**, 2613 (1998).
159. S. Fields and O. Song, *Nature*, **340**, 245 (1989).
160. R. B. Sekar and A. Periasamy, *Cell. Biol.*, **160**, 629 (2003).
161. S. Takeda, A. Ptak, C. Nakamura, J. Miyake, M. Kageshima, S. P. Jarvis and H. Tokumoto, *Chem. Pharm. Bull.*, **49**, 1512 (2001).
162. P. P. Lehenkari and M. A. Horton, *Biochem. Biophys. Res. Commun.*, **259**, 645 (1999).
163. T. Okada, M. Sano, Y. Yamamoto and H. Muramatsu, *Langmuir*, **24**, 4050 (2008).
164. J. M. Kim, R. Yamasaki, J. W. Park, H. S. Jung, H. Y. Lee and T. Kawai, *J. Biosci. Bioeng.*, **97**, 138 (2004).
165. H. Wang, R. Bash, J. G. Yodh, G. L. Hager, D. Lohr and S. M. Lindsay, *Biophys. J.*, **83**, 3619 (2002).
166. J. L. Hutter and J. Bechhoefer, *Rev. Sci. Instrum*, **64**, 1868 (1993).
167. H. G. Lee and E. Fritsche, *Chromatogr.*, **994**, 213 (2003).
168. N. M. Green, *Meth. Enzymol.*, **184**, 51 (1990).
169. S. Freitag, I. L. Trong, L. A. Klumb, V. Chu, A. Chilkoti, P. S. Stayton and R. E. Stenkamp, *Biomol. Eng.*, **16**, 13 (1999).
170. A. Engel and D. J. Muller, *Nat. Struct. Biol.*, **7**, 715 (2000).

171. U. T. Dürig, D. W. Pohl and F. Rohner, *Appl. Phys.*, **59**, 3318 (1986).
172. H. Heinzelmann and D. W. Pohl, *Appl. Phys.*, **A59**, 89 (1994).
173. U. C. Foscher, U. T. Dürig and D. W. Pohl, *Appl. Phys. Lett.*, **52**, 249 (1988).
174. R. C. Reddick, R. J. Warmack and R. L. Ferrell, *Phys. Pev.*, **B.39**, 767 (1989).
175. E. Betzig and J. K. Trautman, *Science*, **257**, 189 (1992).
176. S. Shalom, K. Lieberman and A. Lewis, *Sci. Instr.*, **63**, 4061 (1992).
177. M. F. vanHulst, M. H. P. Moers, O. F. J. Noordman, R. G. Tack, F. B. Segerink and B. Bölger, *Appl. Phys. Lett.*, **62**, 461 (1993).
178. H. Muramatsu, N. Chiba, T. Umemoto, K. Homma, K. Nakajima, T. Ataka, S. Ohta, A. Kusumi and M. Fujihira, *Ultramicroscopy*, **61** 265 (1995).
179. H. Muramatsu, N. Chiba, K. Homma, K. Nakajima, T. Ataka, S. Ohta, A. Kusumi and M. Fujigira, *Appl. Phys. Lett.*, **66**, 3245 (1995).
180. N. Chiba, H. Muramatsu, T. Ataka and M. Fujihira, *Appl. Phys.*, **34**, 321 (1995).
181. H. Muramatsu, N. Chiba, T. Ataka, S. Iwabuchi, N. Nagatani, E. Tamiya and M. Fujihir, *Optical Review*, **3**, 470 (1996).
182. P. K. Hansma, J. P. Cleveland, M. Radmacher, D. A. Walters, P. E. Hillner, M. Bezanilla, M. Fritz, D. Vie and H. G. Hansma, *Appl. Phys. Lett.*, **64** 1738 (1994).
183. C. A. J. Putman, K. O. V. d. Weft, B. G. D. Grooth, N. F. V. Hulst and J. Greve, *Appl. Phys. Lett.*, **64**, 2454 (1994).
184. M. Dreier, D. Anselmetti, T. Richmond, U. Dammer and H. J. Gfintherodt, *Appl. Phys.*, **76**, 5095 (1994).
185. H. U. G. Weirer, *Hitochem. Cytochem.*, **49**, 939 (2001).
186. P. Norio and C. L. Schildkraut, *Science*, **294**, 2361 (2001).
187. R. C. Dunn, *Chem. Rev.*, **99**, 2891 (1999).
188. A. Lewis, M. Isaacson, A. Harootunian and A. Murray, *Ultramicroscopy*, **13**, 227 (1984).
189. D. W. Pohl, W. Denk and M. Lanz, *Appl. Phys. Lett.*, **44**, 651 (1984).
190. M. L. Bennink, O. D. Scharer, R. Lanaar, K. Sakata-Sogawa, J. M. Schins, B. G. d. Grooth and J. Greve, *Cytometry*, **36**, 200 (1999).
191. J. M. Kim, H. Muramatsu, H. Y. Lee and T. Kawai, *FEBS Lett.*, **555**, 611 (2003).
192. J. M. Kim, T. Ohtani and H. Muramatsu, *Surf. Sci.*, **549**, 273 (2004).
193. J. M. Kim, T. Ohtani, S. Sugiyama, T. Hirose and H. Muramatsu, *Anal. Chem.*, **73**, 5984 (2001).
194. H. Yokota, J. SunWoo, M. Sarikaya, G-v.-d. Engh and R. Aebersold, *Anal. Chem.*, **71**, 4418 (1999).
195. V. V. Demidov, M. V. Yavnilovich, M. D. Frank-Kamenetskii and P. Nielsen, *Proc. Natl. Acad. Sci. U.S.A.*, **92**, 2637 (1995).
196. N. O. Bukanov, V. V. Demidov, P. E. Nielsen and M. D. Frank-Kamenetskii, *Proc. Natl. Acad. Sci. U.S.A.*, **95**, 5516 (1998).
197. J. Lohse, O. Dahl and P. E. Nielsen, *Proc. Natl. Acad. Sci. U.S.A.*, **96**, 11804 (1999).
198. H. Muramatsu, K. Homma, N. Yamamoto and J. Wang, *Mater. Sci. Eng. C*, **12**, 29 (2000).
199. J. Wang, *Nucl. Acids Res.*, **28**, 3011 (2000).
200. S. Neidle, *Anti-cancer Drug Design*, **12**, 433 (1997).
201. R. W. Ruddon, *Cancer biology 3rd edition*, Oxford University Press, New York (1995).
202. M. A. Femino, F. S. Fay, K. Fogarty and R. H. Singer, *Science*, **280**, 585 (1998).
203. H. Muramatsu, J. M. Kim, S. Sugiyama and T. Ohtani, *Rev. Sci. Instrum.*, **74**, 100 (2003).

Isao Karube is Dean, School of Bionics at the Tokyo University of Technology. He is also the Director of Research at the Center of Advanced Bionics, the National Institute of Advanced Industrial Science and Technology. Dr. Karube received his B.S. in Food Science from Tokyo University of Fisheries in 1966, his M.S. and Dr. Eng. in Chemical Engineering from the Tokyo Institute of Technology in 1969 and 1972, respectively. He also holds an honorary doctorate from the University of Lund, Sweden (1994). Dr. Karube is recipient of numerous prizes, awards, and recognitions, including the Division Award of the Chemical Society of Japan (1986), The Honorable Citizen of Ceret, France (1993), The Toyko Prize for Science and Technology (1994), The Invention Prize, Japan Institute of Invention and Innovation (1995), The Takeda Science Award (1996), the Biosensors 2002 Award, and the Commendation of the Minister of Education, Culture, Sports, Science and Technology (2003). Dr. Karube has served on numerous professional editorial boards or editorial advisory boards of many international journals, including Regional Editor of "Journals of Biocatalysis and Biotransformation" and of "Applied Biochemistry and Biotechnology"; Journal of Biotechnology, Current Opinion in Biotechnology, Biotechnology and Bioengineering, Analytical Letters, Electroanalysis, Sensors and Materials, Enzyme and Microbial Technology, and Bio-medical Materials and Engineering. His current research focuses on the development of biosensors, the design and development of DNA and proteome chips, the design and synthesis of biofunctional molecules, environmental bioengineering, and the design of bionics concepts.